International Journal of Greenhouse Gas Control 109 (2021) 103361

Contents lists available at ScienceDirect

International Journal of Greenhouse Gas Control

journal homepage: www.elsevier.com/locate/ijggc

Depressurization of CO_2-N_2 and CO_2-He in a pipe: Experiments and modelling of pressure and temperature dynamics

Svend Tollak Munkejord *, Han Deng, Anders Austegard, Morten Hammer, Ailo Aasen, Hans L. Skarsvåg

SINTEF Energy Research, PO Box 4761 Torgarden, Trondheim NO-7465, Norway

ARTICLE INFO

Keywords:
Carbon dioxide
Depressurization
Decompression
Experiment
Impurities
Thermodynamics
Fluid dynamics

ABSTRACT

To design and operate safe and efficient CO_2-transportation systems for CO_2 capture and storage (CCS), engineers need simulation tools properly accounting for the fluid and thermodynamics of CO_2. As the transportation systems evolve into networks, it becomes important that these tools also account for impurities in the CO_2, which may significantly affect the thermophysical properties, directly impacting system design and safety. Tube-depressurization experiments provide crucial data to develop and validate models describing transient multi-phase multicomponent flow in pipes. In this work, we perform experiments in a new facility with dense and fast instrumentation for both pressure and temperature. One experiment is for CO_2 with 1.8 mol % N_2, and one has 1.92 mol % He, both starting from 12 MPa and 25 °C. In order to quantify the effect of impurities, the experiments are compared to results for pure CO_2 and analysed on the background of simulations. We employ a homogeneous equilibrium model (HEM) augmented in this work to account for the appearance of solid CO_2 in CO_2 mixtures. We observe that the moderate amounts of impurities significantly influence both pressure and temperature dynamics. In particular, the 'pressure plateau', a key quantity for the assessment of running-ductile fracture, increases as much as 4 MPa for CO_2-He compared to pure CO_2. A further insight is that models must account for solid CO_2 in order to capture the correct temperature development as the pressure decreases towards atmospheric conditions.

1. Introduction

In order to mitigate climate change, CO_2 emissions must be reduced, and to attain the required scale, a portfolio of technologies are needed. CO_2 capture and storage (CCS) is regarded as one of the necessary contributions (Edenhofer et al., 2014). By the mid century, therefore, several gigatonnes of CO_2 will need to be transported from the emitters to storage sites each year (IEA, 2017). Much of this transportation will be through pipeline networks. To design and operate safe and efficient transportation systems, engineers need simulation tools properly accounting for the fluid and thermodynamics of CO_2 (Aursand et al., 2013). Here, one needs to consider that the critical point (7.38 MPa, 31.0 °C), above which there is no difference between vapour and liquid, and the triple point (517 kPa, − 56.6 °C), where solid CO_2 forms, are within a range that could be attained during normal operation.

Presently, CCS projects predominantly have strict limits on the allowable impurity content in the CO_2 stream to be transported (see e.g. Equinor, 2019), to the point where the impurities may not significantly affect the thermophysical properties of the CO_2 stream. However, this may be relaxed in the future in order to optimize the system. Moreover, it is envisaged that as CCS is deployed, direct source-to-sink transportation will be superseded by transportation networks with multiple sources (Moe et al., 2020). Then, even if the specifications are strict, variations in supply between the sources may yield different total compositions. Further, off-specification delivery of CO_2 into the network may cause significant amounts of impurities to be present in the system, at least temporarily. Among other things, this could lead to transition from single-phase to two-phase flow, with liquid slugging and operational disturbances as a result. Therefore, models supporting the design and operational procedures of CO_2-transportation systems need to be able to predict the effect of impurities in the CO_2 stream.

In general, existing flow models and tools were developed for other fluids, and may not be accurate for CO_2 and CO_2-rich mixtures. Therefore, since there are few flow data for CO_2 available in the open

* Corresponding author.
E-mail addresses: svend.t.munkejord@sintef.no, stm@pvv.org (S.T. Munkejord).

https://doi.org/10.1016/j.ijggc.2021.103361
Received 4 September 2020; Received in revised form 21 December 2020; Accepted 13 May 2021
Available online 1 June 2021

literature, new high-quality data are a prerequisite to further development. One principal experiment that is needed to develop CO_2-transportation systems is the depressurization of a tube. There are several reasons for this. First, such experiments are relevant for the prediction of running-ductile fracture (RDF), where a defect in the pipeline develops into a crack running along the pipeline (see e.g. Aursand et al., 2016; Mahgerefteh et al., 2012a). This kind of event is a hazard, and pipelines transporting highly pressurized compressible fluids need to be designed to avoid RDF for more than 1–2 pipe sections (DNV, 2012). Second, depressurization experiments can be employed to validate model predictions for a large range of pressures and temperatures along the tube. In particular, during decompression of CO_2, the temperature can attain − 78 °C, a level where several materials have turned brittle. Importantly, tube-depressurization experiments are well defined, and therefore suited for model validation and development.

The majority of pipe or tube depressurization experiments reported so far for CO_2 did not include impurities (Armstrong and Allason, 2014; Botros et al., 2016; Brown et al., 2014; 2013; Cao et al., 2018; Clausen et al., 2012; Guo et al., 2017; 2016; Jie et al., 2012; Teng et al., 2016; Yan et al., 2018), but some works are available (see Munkejord et al., 2016). Cosham et al. (2012) reported pressure data for the decompression of a mixture consisting of CO_2, H_2, N_2, O_2 and CH_4 in a pipe of length 144 m and inner diameter 146 mm. A couple of other tests with impurities were also briefly discussed. The main focus was pressure-wave propagation and design of pipelines to avoid RDF. Mahgerefteh et al. (2012b) studied the experimentally observed and calculated decompression-wave speed for various CO_2-rich mixtures initially in a gaseous phase. It was observed that impurities in the CO_2 stream lowered the phase-transition pressure plateau. This is the opposite of what happens for depressurizations from a dense phase.

Huh et al. (2014) observed the effect of 0, 2, 4 and 8% N_2 in CO_2 during the depressurization of a tube of length 51.96 m and inner diameter 3.86 mm. Pressure and temperature data were compared against simulation results obtained using OLGA®. Relatively large discrepancies were observed, particularly for the temperature.

Drescher et al. (2014) presented pressure and temperature data for the depressurization of a tube of length 141.9 m and inner diameter 10 mm. The fluid considered was CO_2 with 10, 20 and 30% N_2. The experiments showed the effect of varying N_2 content and allowed the observation of dry-out, i.e., the point where the liquid has evaporated so that the temperature starts rising. However, there was some uncertainty due to the relatively slow temperature sensors and the fact that the tube was not straight. Further, the N_2 concentrations were higher than what we expect in CO_2 transportation systems.

Gu et al. (2019) experimentally studied the decompression of a tube of length 14.85 m and internal diameter 15 mm, for different nozzle sizes in the millimetre range, including the effect of N_2 as an impurity.

Botros and co-workers have issued several papers presenting pressure data and discussing the corresponding decompression-wave behaviour, for a test section of length 42 m and inner diameter 38.1 mm. A mixture of 72.6% CO_2, 27.4% CH_4 was considered in Botros et al. (2013). Botros et al. (2017a) reported data for four tests with CO_2 mixtures containing 2–7% Ar, 1–6% O_2 and 0.5–4% N_2. Botros et al. (2017c) considered three mixtures representing plausible compositions stemming from pre-combustion and chemical-looping technologies, with varying amounts of H_2, CH_4, CO, O_2 and N_2. Finally, Botros et al. (2017b) reported results from six tests with N_2, O_2, Ar, CO, H_2 and CH_4, respectively, as primary impurities. The observed decompression-wave velocities were compared to velocities calculated employing different equations of state (EOS), where the GERG-2008 EOS (Kunz and Wagner, 2012) was the most accurate of the ones considered. It can be seen from the results, however, that for many of the mixtures, there was a significant deviation between the calculations and the experiments. There was also a significant deviation for the so-called 'plateau pressure'. This is the pressure at which the decompression-wave speed abruptly decreases – hence the appearance of a plateau in the plots. If the process were at equilibrium, this would correspond to the saturation pressure. One can imagine two main reasons for this discrepancy. First, it could be the failure of the EOS to predict the saturation pressure for the state and mixture in question. Second, perhaps more significantly, it could be that the process is too fast to be in equilibrium. To study this in more detail, accurate temperature observations may help, even though the temperature sensors may not be fast enough to capture the fastest variations.

Furthermore, accurate temperature observations are required in order to develop and validate in-tube heat transfer models needed for transient simulations, and the observed temperatures can also be employed to indicate main features of the flow regime, such as two-phase gas-liquid versus single-phase flow, and the occurrence of e.g. solid CO_2 (dry ice). Hence, in this work, we present both high-resolution pressure and temperature data for the decompression of CO_2-rich mixtures. We consider nitrogen (N_2) and helium (He), as representatives of "medium" and "very light" non-condensable impurities. He is the lightest of all elements in terms of boiling point and critical pressure. N_2 can be present in the CO_2 stream from various capture processes (Porter et al., 2015). CO_2 stemming from pre-combustion processes or captured during natural gas reforming for H_2 production may contain H_2 as an impurity (Streb et al., 2019). In this work we consider He instead, since it is similarly challenging with respect to the thermophysical properties, but without being flammable. In particular, both H_2 and He give a significant expansion of the two-phase area. In this work, we employ and adapt the translated and consistent Peng and Robinson (1976) equation of state (EOS) (tc-PR) by Le Guennec et al. (2016b) to data for CO_2-He. Furthermore, although there are vessel models that take into account the thermodynamics of CO_2 mixtures and solid CO_2 formation, we are not aware of any transient pipeflow models with this capability. See also the review by Shafiq et al. (2020). Previous work on pipeflow models for pure CO_2 addressing the formation of solid CO_2 includes Hammer et al. (2013); Munkejord et al. (2016) and Zheng et al. (2017), Martynov et al. (2018). Here we present, for the first time, a dynamic homogeneous equilibrium model (HEM), augmented to account for equilibria involving CO_2-rich mixtures and solid CO_2. This also allows us to present new phase diagrams for CO_2-rich mixtures including predictions for solid-phase CO_2 in equilibrium with fluid phases.

The experiments were carried out in the ECCSEL Depressurization Facility (ECCSEL, 2020), part of the European CCS Laboratory Infrastructure, that was recently put into operation (Munkejord et al., 2020). The facility was constructed and instrumented to obtain high-resolution and synchronized pressure and temperature data. In the present work, the facility was commissioned for use with non-flammable impurities. Moreover, the experimental data collected can be downloaded in full from Zenodo (Munkejord et al., 2021).

There is a two-way coupling between models and experiments. Evidently, experiments are needed to validate models. Equally important, models enhance the understanding of the phenomena and help the design of the experiments. In the following, we therefore discuss the results with a view to model predictions, both with respect to fluid and thermodynamics.

The main contributions of the present work can be summarized in this way:

- New experimental data for the depressurization of CO_2-rich mixtures in a pipe with dense and fast instrumentation for both pressure and temperature.
  - The data can be downloaded freely.
  - The data support model development and validation, and as a consequence, the deployment of CO_2-transportation systems.
- A transient HEM predicting the formation of solid CO_2 in CO_2 mixtures.
- Interaction parameters for the tc-PR EOS adapted to CO_2-He.

The rest of this paper is organized as follows. Section 2 describes the experimental setup, while the models are reviewed in Section 3. Section

4 presents and discusses the results, while Section 5 concludes the paper.

2. Experimental setup

This section gives an overview of the experimental setup. A more detailed description can be found in Munkejord et al. (2020).

2.1. ECCSEL depressurization facility

Figure 1a shows a schematic view of the ECCSEL depressurization facility, which consists of a test section with a rupture disk at the open end and an auxiliary system for filling and conditioning. The auxiliary system includes gas supply with mass flow controllers, two-stage compression with cooling and heating, a circulation pipeline, and a micro gas chromatograph. The maximum operating pressure of the facility is 20 MPa, and the current design allows experiments with initial temperatures in the range 5 °C to 40 °C.

The test section is made of 11 stainless steel (SS316, EN 1.4401) pipes giving a total length of 61.67 m, as depicted in Fig. 1b. The pipes have an inner diameter of 40.8 mm and outer diameter of 48.3 mm, and the internal surface of the pipes were honed to a mean roughness, R_a, in a range from 0.2 μm to 0.3 μm. In order to achieve a uniform axial temperature, the tube is wrapped by PTC heating cables and insulated with a 60 mm thick glass wool layer. The power output of the heating cables is 1900 W at 20 °C and 950 W at 40 °C. The thermal properties of the pipe and insulation layer are given in Table 1.

An X-scored rupture disk is installed at one end of the test section, together with a disk holder. The depressurization is triggered once the disk ruptures. The disk holder has an inner diameter of 63 mm and the open membrane area of the rupture disk matches the disk holder, which gives a larger opening area than the cross-section area of the tube, to ensure choking at the end flange. Rupture disks with a specified burst pressure of 120 barg ±5% at 22 °C are used.

The test section is connected to the gas supply, and the compression and cooling system for achieving the desired experimental conditions, as described in Munkejord et al. (2020a). In particular, for tests with CO_2-rich mixtures, the composition of the mixture is regulated by the two Bronkhorst mass-flow controllers, of type F-203AV for CO_2 and F-201CV for the secondary gas. Moreover, an Agilent 490 micro gas chromatograph (GC) is installed to measure the resulting composition in the test section.

Table 1
Density and thermal properties of the test section materials.

	Density (kg m^{-3})	Thermal conductivity (W m^{-1} K^{-1})	Specific heat (J kg^{-1} K^{-1})
Pipe steel	8000	15	500
Insulation layer	75	0.032	840

2.2. Instrumentation

The test section is specifically instrumented to capture decompression waves. Sixteen fast-response pressure transducers are flush mounted to the internal surface along the pipe with dense distribution close to the rupture disk, as illustrated in Fig. 1b. The transducers are of type Kulite CTL-190(M). A total of 23 Type E thermocouples are installed for the measurement of the fluid temperature. 11 of them are located at the same axial positions as pressure sensors, at the opposite side of the pipe. The remaining 12 thermocouples are installed at the top, bottom and side of the pipe at four locations in order to capture any stratification of the flow. The locations of all the pressure and temperature sensors on the test section are listed in Table 2. The measurement uncertainty of pressure is 60 kPa and temperature uncertainty is ±0.22 °C. In this work, statistical estimates are given with a confidence level of 95%. Details regarding sensor calibration and uncertainty analysis of pressure and temperature measurement can be found in Munkejord et al. (2020a).

The synchronized pressure and temperature data are obtained by three PXIe modules locked to a common reference clock. The data from the pressure and temperature sensors are logged at 100 kHz and 1 kHz, respectively. The high-frequency data are stored for 9 s, including about 0.3 s before disk rupture and 8.7 s after the rupture. After this period, both pressure and temperature are collected at 50 Hz.

For each test, the reported initial conditions are based on data from

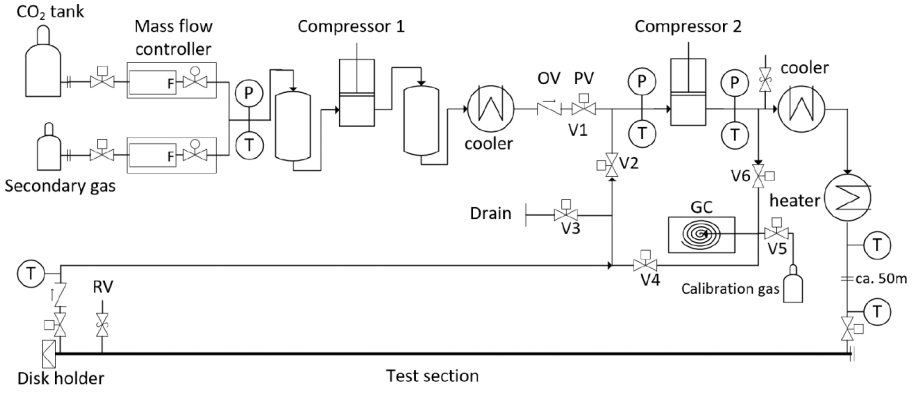

(a) System (RV: relief valve; OV: one-way valve; PV: pneumatic valve)

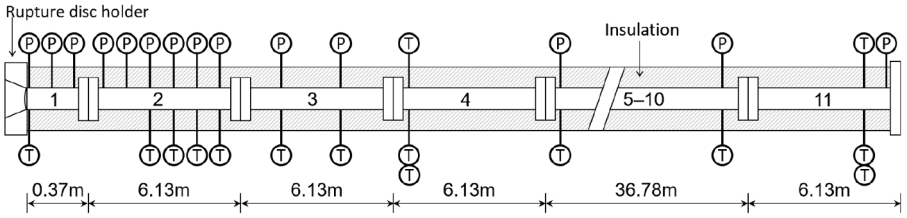

(b) Test section (dimensions are not to scale; pipe no. 5–10 and corresponding sensors are omitted.)

Fig. 1. Schematic of the ECCSEL depressurization facility.

Table 2
Locations of pressure and temperature sensors at 25 °C.

Distance from open end (m)	Pressure sensor	Temperature sensor (side)	Temperature sensor (bottom, side, top)
0.080	PT201	TT201	
0.180	PT202		
0.280	PT203		
0.484	PT204		
0.800	PT205		
1.599	PT206	TT206	
3.198	PT207	TT207	
4.798	PT208	TT208	
6.397	PT209	TT209	
7.996	PT210	TT210	
9.595	PT211	TT211	
15.292			TT241, TT242, TT243
19.990	PT212	TT212	
29.986	PT213	TT213	
30.686			TT251, TT252, TT253
39.984	PT214	TT214	
46.085			TT261, TT262, TT263
49.982	PT215	TT215	
61.280			TT271, TT272, TT273
61.479	PT216		

about 0.5 ms to 1 ms before disk rupture, using the average of the measurements by all the pressure transducers and the length-weighted average of the measurements by the thermocouples at the side of pipe. Specifically, due to the flow configuration during circulation, the temperature is assumed to be piece-wise constant between the rupture disk and TT206 (in Table 2), with a linear variation between TT201 and the circulation outlet at 0.124 m from the open end.

The composition of the CO_2-He mixture was measured with the in-line micro gas chromatograph, while the CO_2-N_2 mixture composition was measured with an off-line gas chromatograph by taking samples manually. The in-line micro gas chromatograph is calibrated with a premixed gas of 98% CO_2 and (2±0.02)% He, and the calibration shows a repeatability of 0.012% in He composition. The off-line gas chromatograph is calibrated with premixed gas of 98% CO_2 and (2±0.02)% N_2, with a repeatability of 0.003% in N_2 composition.

The reported mixture composition is determined from the average value of 4 samples for the CO_2-N_2 test and 65 samples for the CO_2-He test. These samples were taken when the fluid in the test section was in a supercritical or liquid state. The composition uncertainty of N_2 is within 0.2%, while that of He is 0.08%.

2.3. Experimental procedure

For experiments with multiple components, a two-phase vapour-liquid state during filling of the test section may lead to component separation and an ill-defined initial state. Hence we ensured a single-phase state during filling by "circumventing" the two-phase region, see the phase diagrams in Figs. 3 and 4.

The procedure is conducted as follows. (1) The rupture disk is installed and (2) the system is evacuated. (3) The test section is filled with a mixture of gaseous CO_2 and secondary gas heated to 40 °C. (4) The temperature is kept at 40 °C while the mixture is circulated in the test section. The test section is charged using the compressors to a pressure about 1 MPa higher than the highest two-phase pressure of the mixture in the relevant temperature region. (5) The mixture is then cooled to a few degrees below the desired temperature while the fluid is circulated and the pressure is kept constant by further charging. (6) In the final stage, the pressure is increased at a controlled rate until the disk ruptures. (7) After the test, the system is emptied.

The mixture samples are taken from the outlet of the test section during the filling and conditioning steps.

3. Models

In order to obtain a better insight into the experimental results, it is an advantage to be able to discuss them on the background of model calculations. Here we employ the same modelling framework as in Munkejord et al. (2020a). In particular, we account for the formation of solid CO_2 for decompression beyond the vapour-liquid-solid coexistence line. Initial vapour-liquid-equilibrium (VLE) calculations revealed that further work is needed in order to accurately calculate the thermophysical properties of the CO_2-He mixture. We therefore describe in detail how the CO_2-He mixture is modelled.

3.1. Thermophysical properties

To describe the thermodynamic properties, we used different EOSs for the CO_2-N_2 and CO_2-He fluid mixtures. Ideally, the same EOS would be used for both mixtures, but because the most accurate EOS for CO_2-rich mixtures, EOS-CG (Gernert and Span (2016)), does not include a model for the CO_2-He binary mixture, an alternative EOS has been used for that mixture, as discussed below.

In order to model solid CO_2 (dry ice) in equilibrium with the fluid phases, the auxiliary Gibbs free energy EOS of Jäger and Span (2012) was utilized. There are two degrees of freedom in the dry-ice EOS, corresponding to the arbitrary reference state, and these were used to enforce (1) the correct CO_2 triple-point temperature (− 56.558 °C), and (2) the correct enthalpy of melting at this temperature. To achieve this, the triple-point temperature is used to calculate the pure CO_2 saturation pressure from the fluid EOS. At this triple point, the melting enthalpy is set to 8875.0 J mol^{-1}, and the Gibbs free energy of the dry-ice model is set to match the Gibbs free energy of the fluid phases.

According to Gibbs' phase rule, the number of degrees of freedom is zero when having one component and three phases. For pure CO_2 this gives a triple point in temperature-pressure space. With two components and three phases, the number of degrees of freedom becomes one. This means that the triple point becomes a line where three phases coexist. Under the assumption of flow in homogeneous equilibrium, the speed of sound becomes zero for pure CO_2 at the triple point (see e.g. Munkejord et al., 2016), but due to the additional degree of freedom, this is not the case for CO_2 binary mixtures.

Using the composite equation of state, i.e. the fluid model coupled with the auxiliary dry-ice EOS, we can plot the phase behaviour of the binary mixtures. The principles for mapping of phase envelopes are discussed by Michelsen and Mollerup (2007). For an example of how phase envelopes including solid phase can be mapped, we refer to our open-source version of Thermopack (Hammer et al., 2020).

The numerical solution of the HEM (Section 3.2) requires calculation of the most stable phase distribution, temperature and pressure from the conserved variables. This task is called the isoenergetic-isochoric flash. An algorithm for the vapour-liquid-solid equilibrium is part of our in-house thermodynamics library (Wilhelmsen et al., 2017). This library has an interface to the TREND thermodynamic library (Span et al., 2016), which contains an implementation of the EOS-CG and GERG-2008 (Kunz and Wagner, 2012) models. Both EOS-CG and GERG-2008 comprise pure-fluid Helmholtz energy EOSs combined using specialized Helmholtz energy mixture models. The major difference between EOS-CG and GERG-2008 is the use of more accurate pure-fluid EOSs in EOS-CG.

In this work we have included some simulations where the auxiliary solid model is ignored and only the fluid part of the EOS is utilized. In this case, a fictitious vapour-liquid region will exist at temperatures otherwise involving vapour-solid equilibria. The omission of the solid-phase model will influence the phase distribution and thermodynamic properties used for friction and heat-transfer calculations. The main motivation for including the simulations without solid, is to show how the presence of solid influences the results.

3.1.1. CO_2-He binary mixture

GERG-2008 (Kunz and Wagner (2012)) includes the pure-fluid EOS and binary mixture parameters required to model the CO_2-He system. However, comparing the GERG-2008 predictions to available experimental VLE data revealed a poor agreement. In order to use EOS-CG or GERG-2008 with confidence for the CO_2-He system, a new binary mixture model or refitted parameters are required. Such a development would require a major effort and is outside the present scope.

In this work, we therefore used the translated and consistent Peng-Robinson EOS (tc-PR) by Le Guennec et al. (2016b). It is a state-of-the-art cubic EOS, which uses accurate and consistent implementations of the Twu alpha function (Le Guennec et al., 2016a; Twu et al., 1991). It takes the form

$$P(T,v,\boldsymbol{x}) = \frac{RT}{v-b} - \frac{a(T,\boldsymbol{x})}{(v+c)(v+b+2c)+(b+c)(v-b)}, \tag{1}$$

where T, v and $\boldsymbol{x} = (x_1, x_2, \ldots)$ are the temperature, molar volume and mole fraction vector, and R is the gas constant.

For pure components, the attractive energy parameter a can be written as $a = a_{\mathrm{cr}}\alpha(T)$, where the α function is regressed to saturation pressures, enthalpies of vaporization, and saturated liquid heat capacities. The critical energy parameter a_{cr}, the covolume b and the Péneloux volume-shift parameter c are chosen to exactly reproduce the component's experimental critical temperature T_{cr}, critical pressure P_{cr}, and saturated liquid density at the temperature $T = 0.8T_{\mathrm{cr}}$. These parameters are given in Le Guennec et al. (2016b), except for one modification we have made for the Péneloux volume-shift parameter c for He. The c parameter is usually fitted to yield more accurate predictions of saturated liquid densities (Péneloux et al., 1982), but since the saturation of pure He only occurs at extremely low temperatures ($T_{\mathrm{cr}}(\mathrm{He}) = 5.2$ K) we have removed it, i.e. set $c_{\mathrm{He}} = 0$. However, the volume shift parameter of tc-PR for CO_2 was retained; $c_{\mathrm{CO_2}} = -1.1368 \times 10^{-6}$ m^3 mol^{-1}.

For mixtures, the parameters a, b and c are calculated as

$$a(T,\boldsymbol{x}) = \sum_i \sum_j x_i x_j a_{ij}, \quad a_{ij} = \sqrt{a_{ii}a_{jj}}\left(1-k_{ij}\right), \tag{2}$$

$$b(\boldsymbol{x}) = \sum_i x_i b_i, \tag{3}$$

$$c(\boldsymbol{x}) = \sum_i x_i c_i, \tag{4}$$

where a_{ii}, b_i and c_i are the parameters for pure component i, and k_{ij} is the binary interaction parameter.

We fitted the binary interaction parameter to experimentally measured VLE compositions and single-phase densities. The composition measurements were taken from Burfield et al. (1970), Liu (1969), Mackendrick et al. (1968), and the density measurements were those from Kesselman and Alekseenko (1974), Kosov and Brovanov (1975) that were below 200 bar and below 500 K. The objective function O was chosen as a weighted sum of total absolute deviations of measured (superscript expt) and calculated (superscript calc) mole fractions, and the relative error in predicted densities:

$$O\left(k_{ij}\right) = \frac{1}{N_x+N_y}\left(W_x \sum_{i=1}^{N_x} |x_i^{\mathrm{expt}} - x_i^{\mathrm{calc}}| + W_y \sum_{i=1}^{N_y} |y_i^{\mathrm{expt}} - y_i^{\mathrm{calc}}|\right) + \frac{W_\rho}{N_\rho} \sum_{i=1}^{N_\rho} \frac{|\rho_i^{\mathrm{calc}} - \rho_i^{\mathrm{expt}}|}{\rho_i^{\mathrm{expt}}}. \tag{5}$$

Here x_i and y_i are, respectively, the mole fractions of He in the liquid and the vapour, i indexes the states where the deviations are calculated, N_x, N_y and N_ρ are the number of measurements of liquid compositions, vapour compositions and densities, and W_x, W_y and W_ρ are weighting factors adjusted to yield a reasonable tradeoff between accuracy in the predictions for the different properties. The EOS calculations were performed at the same temperature and pressure as reported in the experiments.

The optimal binary interaction parameter was found to be $k_{\mathrm{CO_2,He}} = 0.556$, and Table 3 shows the details of the objective function and the resulting accuracy for the mixture compositions and densities. Figure 2 shows that agreement for VLE compositions is much better compared to GERG-2008. Figure 3 illustrates the calculated temperature-pressure VLE envelope for a mixture of 98.08 mol % CO_2 and 1.92 mol % He from the two EOSs, showing significant differences, especially for the liquid branch.

3.1.2. CO_2-N_2 binary mixture

For the CO_2-N_2 mixture, EOS-CG gives accurate results. However, due to the high computational cost of EOS-CG, it is also relevant to consider the classical Peng and Robinson (1976) (PR) EOS. This amounts to employing (1) with $c = 0$, using the original PR α-correlation. The CO_2-N_2 binary interaction parameter, for the van der Waals mixing rules in (2), is set to $k_{\mathrm{CO_2,N_2}} = 0.022$. The interaction parameter was tuned to match the VLE phase envelope behaviour of EOS-CG for the specific binary mixture used in this work. The temperature-pressure phase diagram for the 98.2 mol % CO_2 and 1.8 mol % N_2 mixture is shown in Fig. 4.

3.1.3. Transport properties

To account for heat transfer and friction, models are needed for the viscosity and the thermal conductivity. In this work, the fluid-phase thermal conductivity and dynamic viscosity are calculated using an extended corresponding-state method with propane as the reference fluid (Ely and Hanley, 1981; 1983). As the volume fraction of solid is always small, the effect of dry ice on viscosity and thermal conductivity is neglected.

3.2. Transient multiphase multicomponent flow model

In this work, we represent the transient compressible single-, two- or three-phase flow of CO_2-rich mixtures employing a homogeneous equilibrium model (HEM). Herein, the different phases are assumed to exist in mechanical, kinetic, thermal and chemical equilibrium at all times, i.e., the phases have the same pressure, velocity, temperature and chemical potential. This represents some physical simplifications, but it nevertheless requires a particularly robust calculation of the thermophysical properties. The model was discussed in detail by Munkejord and Hammer (2015), Munkejord et al. (2016) and we review it here for completeness.

3.2.1. Governing equations

The governing equations have the same form as the Euler equations for single-phase compressible inviscid flow, and consist of a mass-conservation equation,

$$\frac{\partial}{\partial t}(\rho) + \frac{\partial}{\partial x}(\rho u) = 0, \tag{6}$$

a momentum-balance equation,

$$\frac{\partial}{\partial t}(\rho u) + \frac{\partial}{\partial x}\left(\rho u^2 + P\right) = \rho g_x - \mathscr{F}, \tag{7}$$

and a balance equation for the total energy,

Table 3
Binary fitting campaign for CO_2-He. Angle brackets indicate averages, and the superscripts "abs" and "rel" indicate whether absolute or relative deviations were used in the averaging.

N_x	W_x	$\langle\lvert\Delta^{\mathrm{abs}}x\rvert\rangle$	N_y	W_y	$\langle\lvert\Delta^{\mathrm{abs}}y\rvert\rangle$	N_ρ	W_ρ	$\langle\lvert\Delta^{\mathrm{rel}}\rho\rvert\rangle$
71	100	0.0019	92	100	0.0081	12	50	1.32%

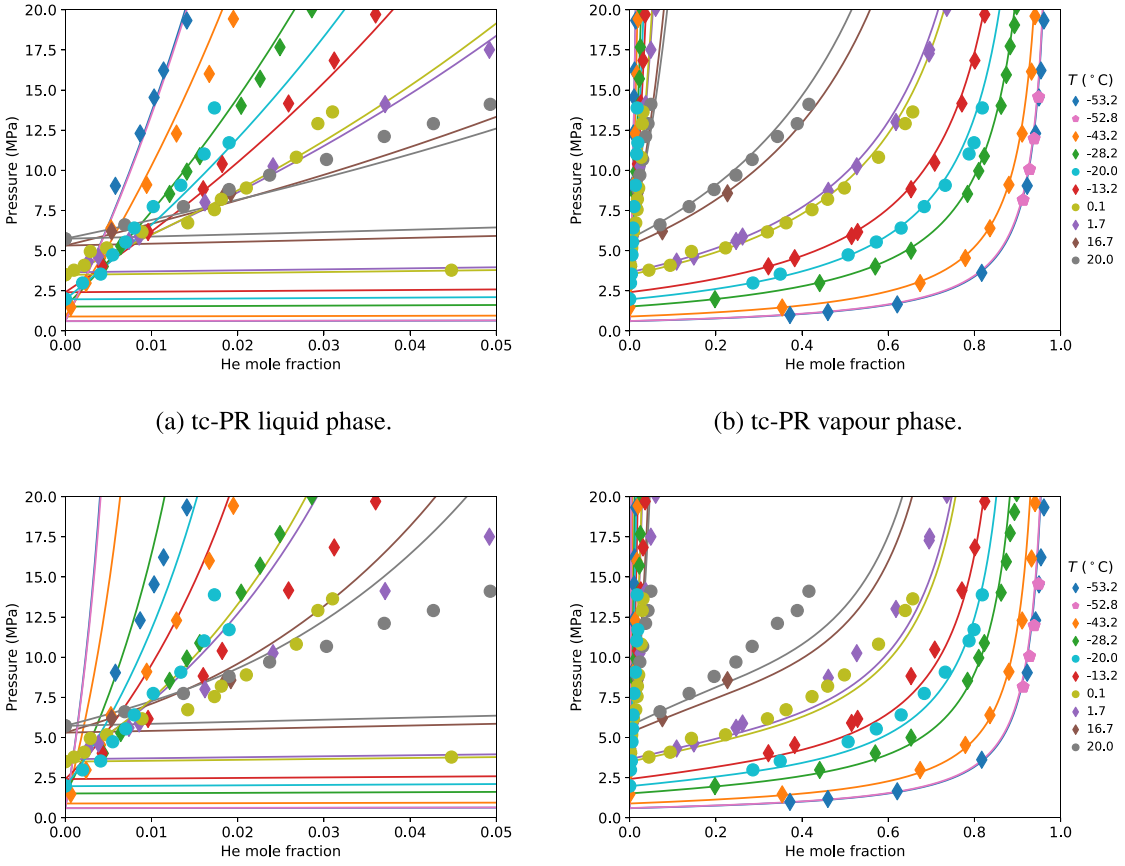

(a) tc-PR liquid phase. (b) tc-PR vapour phase.

(c) GERG-2008 liquid phase. (d) GERG-2008 vapour phase.

Fig. 2. Isothermal pressure–composition phase envelopes for the CO_2-He mixture, computed with the tc-PR EOS (Fig. 2a and b) and GERG-2008 (Fig. 2c and d). Experimental data (symbols) from Burfield et al. (1970), Liu (1969), Mackendrick et al. (1968). The different colours correspond to different temperatures, as given in the legend on the right.

$$\frac{\partial}{\partial t}(E)+\frac{\partial}{\partial x}u(E+P)=\rho g_x u+\mathscr{Q}. \tag{8}$$

Herein, $\rho=\alpha_g\rho_g+\alpha_\ell\rho_\ell+\alpha_s\rho_s$ is the density of the gas (g), liquid (ℓ) and solid (s) mixture. u is the common velocity and P is the pressure. $E=\rho(e+1/2u^2)$ is the total energy density of the mixture, while $e=(e_g\alpha_g\rho_g+e_\ell\alpha_\ell\rho_\ell+e_s\alpha_s\rho_s)/\rho$ is the mixture specific internal energy. α_k denotes the volume fraction of phase $k\in$ g,ℓ,s. $\mathscr{F}$ is the wall friction and $\mathscr{Q}$ is the heat transferred through the pipe wall to the fluid. g_x is the gravitational acceleration in the axial direction of the pipe.

3.2.2. Wall-friction model

The wall friction, $\mathscr{F}$, is calculated as follows.

$$\mathscr{F}=\begin{cases} f_k\dfrac{\dot m|\dot m|}{2\rho_k d_i} & \text{for single-phase flow,}\\ f_\ell\dfrac{\dot m|\dot m|}{2\rho_\ell d_i}\Phi & \text{for two-phase flow,}\end{cases} \tag{9}$$

where $f_k=f(Re_k)$ is the Darcy friction factor, $Re_k=|\dot m|d_i/\mu_k$ is the Reynolds number for phase k, $\dot m=\rho u$ is the mass flux, and d_i is the inner pipe diameter. The coefficient Φ is an empirical correlation, which is used to account for two-phase flow, and it depends on various properties of both phases. Here we have employed the Friedel (1979) correlation. Details of the calculation of the two-phase coefficient Φ, and also further discussion, can be found in Aakenes (2012), Aakenes et al. (2014).

3.2.3. Heat-transfer model

The heat flux per fluid volume, $\mathscr{Q}$, accounts for radial heat conduction from the tube to the fluid. It is given by

$$\mathscr{Q}=\frac{2h_i}{r_i}(T_i-T), \tag{10}$$

where r_i is the tube inner radius, h_i is the fluid-wall heat-transfer coefficient, T_i is the tube inner wall temperature and T is the fluid temperature. To calculate T_i, we assume that the temperature profile in the tube wall and the surrounding insulation is radially symmetric, and the axial heat conduction can be neglected. In this way, the heat transfer from the ambient air through the insulation and the tube to the fluid is accounted for. See Aursand et al. (2017) for further details on the treatment of radial conduction through multiple layers. In the cases we consider, the radial temperature is varying with time. Therefore, the heat equation needs to be solved along with the flow model. It reads

$$\rho(r)c_p(r)\frac{\partial T}{\partial t}-\frac{1}{r}\frac{\partial}{\partial r}\left(\lambda(r)r\frac{\partial T}{\partial r}\right)=0, \tag{11}$$

where $\rho(r)$, $c_p(r)$ and $\lambda(r)$ are the density, specific heat capacity and thermal conductivity, respectively, at radial position r.

To calculate the inner heat-transfer coefficient, h_i, we employ the following correlation for the Nusselt number, Nu,

$$Nu=\begin{cases}3.66 & Re<2300,\\ 0.023Re^{4/5}Pr^{p} & Re>3000,\end{cases} \tag{12}$$

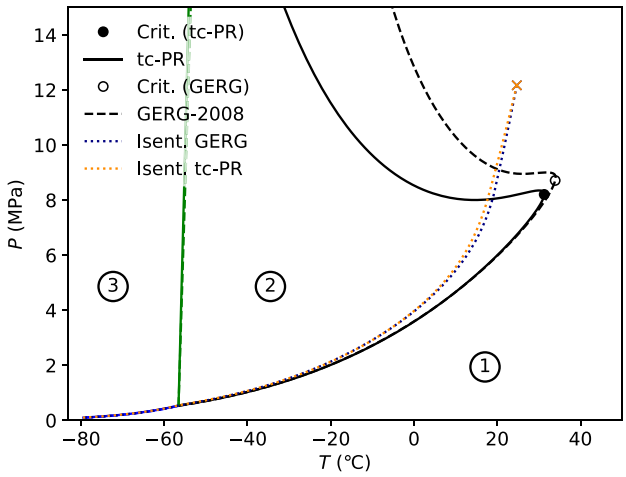

Fig. 3. Temperature–pressure phase diagram for a mixture of 98.08 mol % CO_2 and 1.92 mol % He, computed with the tc-PR (solid lines) and GERG-2008 (dashed lines) equations of state and the auxiliary dry-ice Gibbs free energy model of Jäger and Span. The blue curve is the sublimation curve, the black curve is the two-phase vapour-liquid envelope, and the green curve is the vapour-liquid-solid coexistence curve. In area ① of the diagram a single phase is stable, for area ② vapour and liquid coexist, while in area ③ vapour and solid coexist. The isentrope starting from the initial conditions listed in Table 4, is included for both the tc-PR and GERG-2008. (For interpretation of the references to colour in this figure legend, the reader is referred to the web version of this article.)

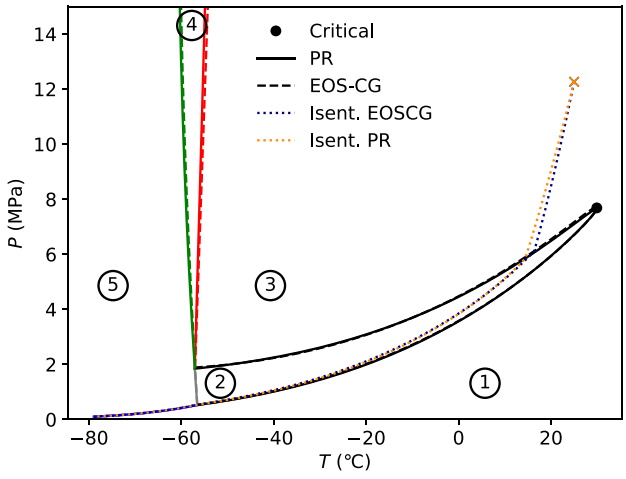

Fig. 4. Temperature–pressure phase diagram for a mixture of 98.2 mol % CO_2 and 1.8 mol % N_2, computed with the PR (solid lines) and EOS-CG (dashed lines) equations of state and the auxiliary dry-ice Gibbs free energy model of Jäger and Span. The blue curve is the sublimation curve, the black curve is the two-phase vapour-liquid envelope, the red curve is the solid-liquid melting line, the grey line is the vapour-liquid-solid coexistence line and the green curve is the saturation line where the liquid phase, depleted with CO_2, transitions into a N_2-rich vapour phase. Vapour is the stable phase in area ① of the diagram. In area ② vapour and liquid coexist. Liquid is the stable phase in area ③. In area ④ liquid and solid coexist. In area ⑤ vapour and solid coexist. The isentrope starting from the initial conditions listed in Table 4, is included for both the PR and EOS-CG. (For interpretation of the references to colour in this figure legend, the reader is referred to the web version of this article.)

with linear interpolation in the region $2300 \leq Re \leq 3000$. The second line is the Dittus-Boelter correlation, see e.g. Bejan (1993, Chap. 6). Herein, $p = 0.4$ when the fluid is heated and $p = 0.3$ when the fluid is cooled. The Nusselt number, Nu, and the Prandtl number, Pr, are defined as

$$Nu = \frac{h_i d_i}{\lambda_m}, \quad Pr = \frac{c_{p,m}\mu_m}{\lambda_m}, \tag{13}$$

where subscript m indicates fluid mixture properties. The mixture viscosity and thermal conductivity are calculated as a volume average of the phase properties. To account for the enhanced heat transfer due to boiling, the correlation of Gungor and Winterton (1987) is chosen for its simplicity. The heat flux, q (W m^{-2}), correlation is implicitly formulated,

$$q = q(h_i(q), T_w, T). \tag{14}$$

We calculate the heat-transfer coefficient in an explicit manner based on the fluid solution at time step n and the heat flux from time step $n-1$. Regarding the outside heat-transfer coefficient, it is assumed to be 4W m^{-2} K^{-1}.

3.2.4. Numerical solution

For the numerical solution we employ the finite-volume method, where the numerical fluxes are calculated using the first-order centred (FORCE) scheme (Toro and Billett, 2000). As described by Hammer et al. (2013), we obtain second order by using the monotone upwind-centred scheme for conservation laws (MUSCL) and a strong-stability-preserving Runge-Kutta method.

For the simulations performed in this work, we employed a Courant-Friedrichs-Lewy (CFL) number of 0.85. For calculations shorter than 0.2 s, we used a spatial grid of 4800 cells, whereas for longer times, 1200 cells were used.

3.3. Decompression-wave speed

The decompression-wave speed is a main quantity in the assessment of running-ductile fracture (RDF) in pipelines transporting CO_2 or other pressurized and compressible fluids, see e.g. Aursand et al. (2016).

The decompression-wave speed can be extracted from the HEM simulations. However, a simplified method can be employed, giving very similar results, see the discussion in Aursand et al. (2016). For one-dimensional isentropic flow, the decompression-wave speed for a fully-developed wave at a pressure level, P, along an isentrope, can be calculated by

$$v(P) = c(P) - \int_P^{P_i} \frac{1}{\rho(P')c(P')}\,\mathrm{d}P', \tag{15}$$

where c is the speed of sound and P_i is the initial pressure. For two-phase states, full equilibrium is most often assumed, analogous to what is done in the HEM. In the following, we will also present calculations without phase transfer, i.e., the fluid remains in a meta-stable state. Since the expression (15) is evaluated using an EOS, comparing the experimentally determined wave speeds with those calculated using (15) constitutes a test of the EOS, at least for single-phase states.

The speed of sound can be calculated from the relation

$$c = \sqrt{\left(\frac{\partial P}{\partial \rho}\right)_s}, \tag{16}$$

where the subscript s indicates that the differential is isentropically constrained. For a multiphase mixture, the pressure differential is also subject to constraints maintaining equilibrium between the phases. In this work we employ analytic differentials.

4. Results and discussion

In order to study the effect of impurities on the decompression behaviour of a CO_2 stream, we retain the conditions of Test 8 for pure CO_2, reported in Munkejord et al. (2020a). The nominal conditions are

Table 4
Experimental conditions of the depressurization tests of CO_2-rich mixtures.

Test no.	Impurity	Concentration (mol %)	Pressure (MPa)	Temperature (°C)	Ambient temp. (°C)	PT5 temp. (°C)	Figures
8[a]	none	N/A	12.22	24.6	9	24.3	7,11, 15
9	N_2	1.8	12.27	25.0	4	24.1	5,7, 9, 11,12, 15
12	He	1.92	12.17	24.7	6	24.4	6,7,10, 11,14, 15

[a] From Munkejord et al. (2020a).

12 MPa and 25 °C, see Table 4. Here we report on one experiment with 1.8 mol % N_2 (Test 9) and one with 1.92 mol % He (Test 12). For convenience, the figures containing data from each experiment are listed.

4.1. Pressure

We first consider Test 9 for CO_2-N_2. Figure 5 displays measured and simulated pressure at the sensor positions. Simulations employing EOS-CG (dashed lines) and the PR EOS (dotted lines) are shown. The whole decompression process is shown in Fig. 5a, whereas Fig. 5b concentrates on the first instants where the transients are fast. As can be observed from Fig. 5b, upon arrival of the first decompression wave, the pressure sensors experience an abrupt pressure reduction. At about 6 MPa at the outlet (and increasing upstream due to friction and heat transfer, see the discussion in relation to Fig. 10 in Munkejord et al. (2020a)), the pressure traces level off for a shorter or longer period depending on the position, and the decompression proceeds slower. This corresponds to the onset of two-phase flow, as is also illustrated in the phase diagram in Fig. 4.

In Fig. 5, simulation results obtained with the homogeneous equilibrium model (HEM) are plotted along with the experimental values. It can be observed that close to the outlet and during the first instants of depressurization, the HEM tends to overestimate the pressure 'plateau', something which could be related to non-equilibrium effects, which will be further discussed in the next section. Later, and further upstream, the pressure-plateau levels match relatively well, see e.g. sensor PT209 at 0.1 s (Fig. 5d). Even later, see Fig. 5a at about 3 s, there is an overestimation of the pressure. At this point, the outlet boundary condition and the assumption of a highly dispersed flow, which does not hold in all the pipe, play a role. All in all, however, we find that the HEM performs well, given its simplifications. Furthermore, Fig. 5d illustrates that the PR EOS underestimates the speed of sound (later wave arrival times), and more so for high pressures. EOS-CG, on the other hand, gives accurate values in the single-phase region. In Fig. 3 in Munkejord and

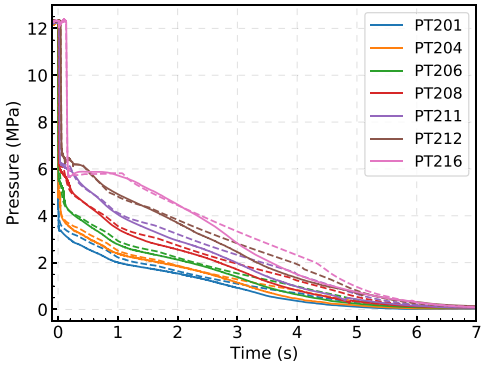

(a) Full depressurization, experiments and simulations using EOS-CG.

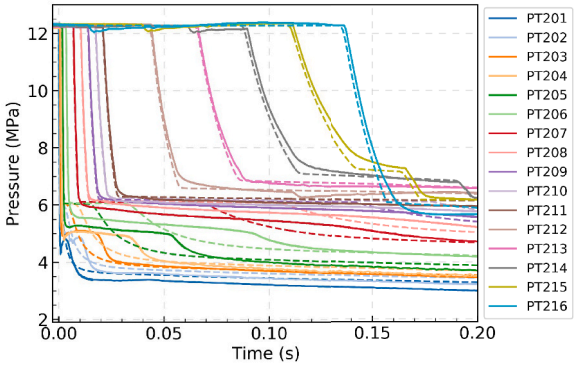

(b) First 0.2 s, experiments and simulations using EOS-CG.

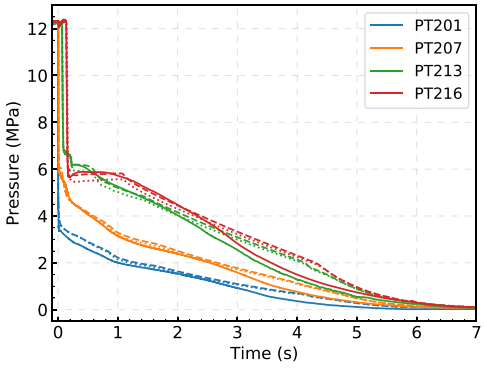

(c) Full depressurization, experiments and comparison between simulations using EOS-CG (dashed lines) and the PR EOS (dotted lines).

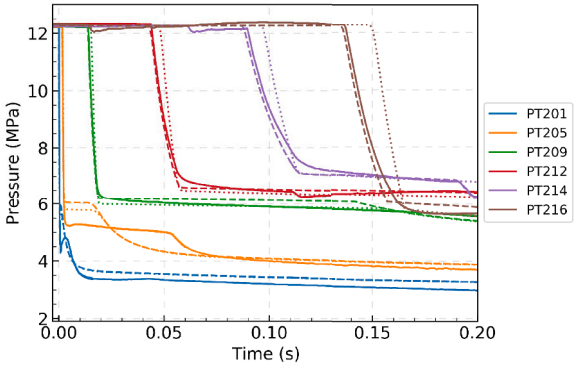

(d) First 0.2 s, experiments and comparison between simulations using EOS-CG (dashed lines) and the PR EOS (dotted lines).

Fig. 5. Measured (full lines) and simulated pressure, with EOS-CG (dashed lines) and with PR (dotted lines), at the sensor positions, for Test no. 9.

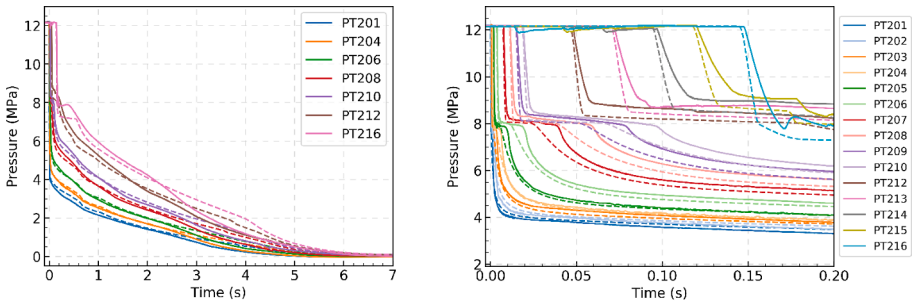

(a) Full depressurization. (b) First 0.2 s.

Fig. 6. Measured (full lines) and simulated pressure (dashed lines) for Test no. 12.

Hammer (2015), we reported that the PR EOS underestimated the single-phase speed of sound for a different CO_2-rich mixture. It can also be seen from Fig. 5d that in the current case, PR gives a longer duration of the pressure plateau than EOS-CG. This difference increases upstream and is due to the difference between the liquid speed of sound and the two-phase mixture speed of sound.

The difference between predictions obtained using EOS-CG and those for the PR EOS are further illustrated by the plot in Fig. 5c for the whole depressurization. It can be seen that after the initial strong transients, the difference is limited. This is due to the fact that the benefit of using EOS-CG over a cubic EOS is mainly the improved density and speed-of-sound predictions. The cubic EOS, however, will predict VLE and energetic properties with satisfactory accuracy. For the initial strong transient plotted in Fig. 5d, the density and speed of sound will define the rarefaction-wave velocity according to (15). For the 'slower' effects plotted in Fig. 5c, when the fluid is in a two-phase state, VLE, energetic properties, heat transfer to the fluid and friction will all have an effect, through the coupling of mass, momentum and energy.

The measured and simulated pressure for Test 12 with CO_2-He is displayed in Fig. 6. For Test 12, our simulations are carried out employing the tc-PR EOS described in Section 3.1.1. Overall, the trends are similar to those for Test 9 in Fig. 5. However, when comparing the experimental results in Fig. 6b with those in Fig. 5b, we see that the pressure 'plateau' is significantly higher, at about 8 MPa at the outlet compared to about 6 MPa for Test 9. As illustrated in the phase diagram in Fig. 3, this is mainly due to the larger two-phase area of CO_2-He compared to CO_2-N_2. Further, it can be observed that the HEM with tc-PR predicts the pressure wave well at 12 MPa. Although the interaction parameter for tc-PR was not tuned to speed of sound data, at this pressure the speed of sound prediction happens to be very accurate. For lower pressures, however, the simulated pressure drops too early, i.e., the speed of sound is too high. We also observe that the experimental pressure traces in the two-phase area (below the 'plateau') vary more gradually in Test 12 than in Test 9 during the first instants of the depressurization, close to the outlet.

The effect of impurities on the observed pressure during decompression is illustrated in Fig. 7 by plotting experimental values for Tests 8 (dark – pure CO_2), 10 (medium colour – CO_2-N_2) and 12 (light – CO_2-He) for three sensors. As can be seen from Fig. 7a, the pressure drops faster and deeper for CO_2. At the position of PT213, the 'plateau' pressure goes up from about 5.8 MPa for pure CO_2 to 6.7 MPa for CO_2-N_2 and further to 8.8 MPa for CO_2-He. The later arrival of the pressure dip for Tests 9 and 12 means that the impurities decrease the speed of sound of the CO_2 stream. A further interesting effect can be observed in Fig. 7b. At about 1.5 s, there is an 'inversion', i.e., the pure-CO_2 experiment changes from the lowest to the highest pressure, and the other way around for the CO_2-He experiment. This is also seen in our simulations, see Fig. 8. There are two main effects governing the pressure 'inversion'. First, the initial pressure drop is a function of the phase-transition pressure, which is lowest for CO_2. Second, CO_2 with N_2 and He have a higher mixture speed of sound, which gives a higher mass outflow rate, so that the pressure for Test 9 and 12 catch up with that of Test 8.

4.2. *Decompression-wave speed*

As mentioned in Section 3.3, the decompression-wave speed is a

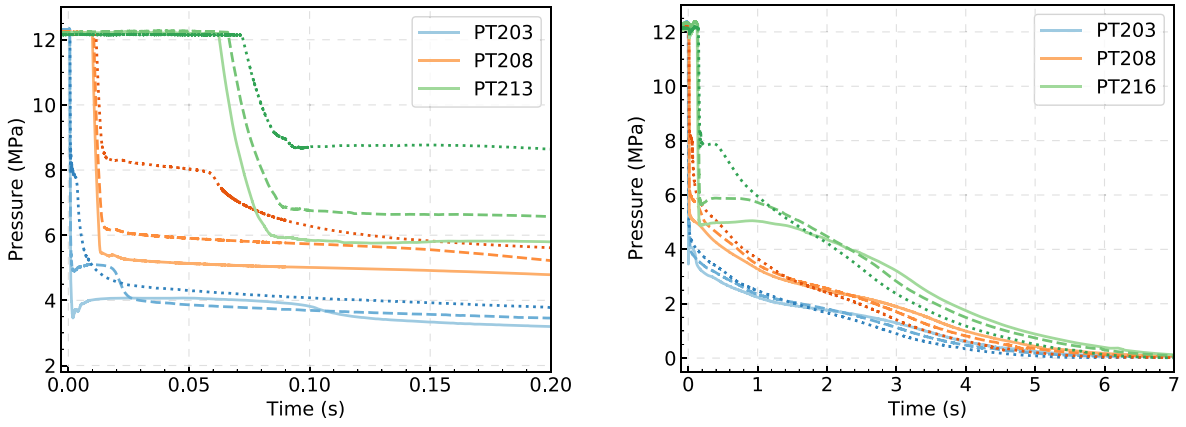

(a) First 0.2 s. (b) Complete depressurization, 7 s.

Fig. 7. Measured pressure for different positions – effect of impurities. Comparison of Test no. 8 (lightest colours, solid line – CO_2), 9 (medium colours, dashed line – CO_2-N_2) and 12 (darkest colours, dotted line – CO_2-He).

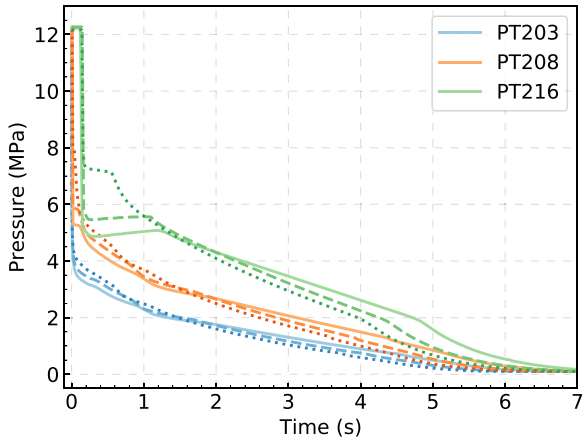

Fig. 8. Simulated pressure for different positions – effect of impurities. Comparison of Test no. 8 (lightest colours, solid line – CO_2), 9 (medium colours, dashed line – CO_2-N_2) and 12 (darkest colours, dotted line – CO_2-He).

main quantity in the assessment of running-ductile fracture (RDF) in pipelines transporting CO_2 or other pressurized and compressible fluids. Of particular interest is the pressure at which the decompression-wave speed shifts from fast propagation in the liquid phase to slow propagation in the two-phase fluid. This pressure is often referred to as the 'plateau pressure', for reasons evident from the graphs in the following.

The decompression-wave speed can be determined from the experimentally recorded pressure as the slope of the linear fit of the sensor locations and the wave arrival time, as described by Botros et al. (2010, 2016, 2007). Here we employ the first five pressure sensors, i.e., a portion of the test section in which friction and heat transfer has not had time to act. We will compare the experimentally determined wave speeds to model calculations employing (15). The initial temperature for the calculations is the length-weighted average temperature from the open end to the fifth pressure sensor, which is given as 'PT5 temp.' in Table 4.

Figure 9 displays wave speeds for Test 9 (CO_2-N_2). The legend 'equilibrium' (blue) refers to full thermodynamic equilibrium for two-phase states, whereas for 'liquid' (green), the fluid remains in a meta-stable liquid state. The curve for 'liquid' ends at the point where the isentrope reaches the spinodal. It can be seen that when full thermodynamic equilibrium is assumed, the decompression-wave speed abruptly decreases from about 350 m s^{-1} to 40 m s^{-1} at 6 MPa. This corresponds to the bubble point predicted by the EOS (EOS-CG). We observe that the experiments indicate a more gradual phase transition at a lower pressure, about 5 MPa, and with a pressure slope instead of a plateau. In the figure, the dotted line connects the two regions where we could extract experimental data. A second observation is that the experimental data lie between the calculations for equilibrium and those for a meta-stable liquid, although somewhat closer to equilibrium. Finally, we observe that in the single-phase liquid (high pressure) region, there is very good agreement between the experiment and calculations (and hence EOS-CG).

In our interpretation, the fact that the experiment shows a lower phase-transition pressure than that calculated using EOS-CG does not mean that the EOS-CG incorrectly predicts the bubble-point pressure. Rather, this means that the process is so fast that equilibrium does not have time to establish itself. For example, at the first pressure sensor, it takes about 210 μs for the pressure to drop from the initial value to 5.3 MPa. During a running-ductile fracture (RDF), the phase-transition pressure (boiling pressure) drawn in Fig. 9 determines the load on the opening pipe flanks. Therefore, employing the saturation pressure, which is higher than the observed pressure, in RDF assessments, is conservative (Cosham et al., 2012). This does, however, not mean that the Battelle two-curve method is conservative as such (Jones et al., 2013).

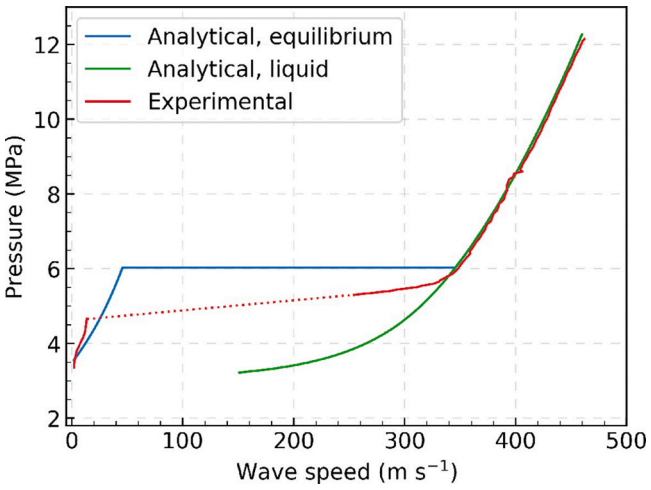

Fig. 9. Measured and calculated wave speed for Test no. 9.

The decompression wave speeds for Test 12 (CO_2-He) are plotted in Fig. 10. The experimental values are plotted in red, whereas the blue colour here denotes values calculated using the tc-PR EOS and the green colour denotes values calculated using the GERG-2008 EOS. It can be seen that although tc-PR has been adapted to available data, it gives the wrong slope in the single-phase area, and judging from the case of CO_2-N_2 in Fig. 9, the bubble-point pressure appears to be too low. GERG-2008, on the other hand, has about the right slope in the single-phase area, but the wave-speed values are about 25 m s^{-1} too high, and the bubble-point pressure also appears to be too high. Since the experimental and modelled decompression-wave speed for CO_2-N_2 in Fig. 9 match very well, we can infer from (15) that the single-phase density and speed-of-sound predictions by EOS-CG are of high accuracy. As can be seen from the results in Munkejord et al. (2020a), the same applies to pure CO_2.

The effect of impurities on the decompression-wave speed is summarized in Fig. 11 by plotting the experimental data from Tests 8 (CO_2), 9 (CO_2-N_2) and 12 (CO_2-He) together. Compared to the case of pure CO_2, CO_2-N_2 has a 25 m s^{-1} lower single-phase (liquid) decompression-wave speed and a 1 MPa higher phase-transition pressure, whereas CO_2-He has 65 m s^{-1} lower single-phase decompression-wave speed and a 3.75 MPa higher phase-transition pressure. These values are significant and need to be taken into account in several design situations, in particular

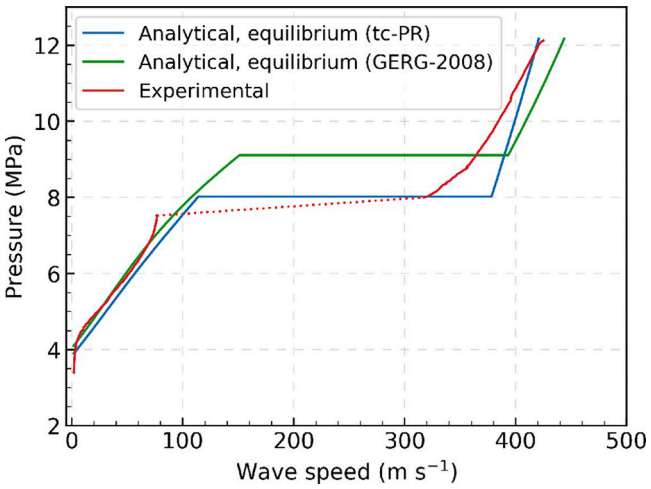

Fig. 10. Measured and calculated wave speed for Test no. 12.

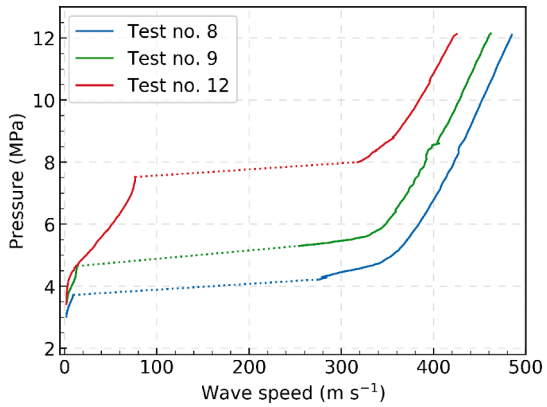

Fig. 11. Measured wave speed for Test no. 8 (CO_2), 9 (CO_2-N_2) and 12 (CO_2-He).

for the assessment of RDF.

4.3. Temperature

Temperature measurements are essential in order to validate the heat-transfer models needed in pipeflow simulations. Furthermore, as will be discussed, the temperature measurements can indicate the occurrence of separated gas-liquid flow regimes and solid-CO_2 formation.

Figure 12 shows measured and simulated temperatures for Test 9 (CO_2-N_2) for different positions. For the simulations, the PR EOS was employed with and without accounting for solid CO_2. Fig. 12a shows the temperature at a position 8 cm from the outlet. Within 30 ms, the measured temperature drops from the initial temperature to below 0 °C. Thereafter, the temperature steadily falls down to − 60 °C at about 4.5 s, and then it starts rising. That is, this is the dry-out point at which there is no liquid left. The temperature-drop trend, including the time of dry-out, is very well captured by the HEM. This indicates that the flow at the outlet is highly dispersed as presumed by the HEM. From about 3 s until dry-out, the simulation starts overpredicting the temperature. After dry-out, there is also good agreement between the experiment and the simulation, although with an underprediction.

Figures 12 b and c show the temperatures recorded at about 15 m from the outlet and from the closed end, respectively. Here, we have three temperature sensors, oriented close to the top, side and bottom of the tube, indicated with increasing line darkness in the figures. In Fig. 12b, we observe that the three temperature sensors give very similar readings. In Fig. 12c, further upstream, the top sensor indicates dry-out about 1 s earlier than the side and bottom sensors. We interpret this to be due to some degree of gas-liquid flow separation. Also dry-out occurs later at the upstream position than the downstream one. At both these positions, the HEM predicts dry-out somewhat early. This is consistent with the assumption of no phase slip in the HEM, meaning that too much liquid is transported away, leading to early dry-out.

In Fig. 12c we make an interesting observation regarding solid CO_2. The temperature simulated without solid CO_2 increases monotonically after dry-out, whereas the one with solid CO_2 experiences a second drop at about 7 s. The measured temperature has a similar qualitative development. Our interpretation is that the temperature drop is due to solid CO_2 having been formed upstream, influencing the heat transfer from the wall. Furthermore, the model without solid CO_2 employs a fictitious vapour-liquid region at low temperatures and pressures, leading to the use of a high two-phase gas-liquid heat-transfer coefficient, and consequently higher temperatures.

This is further illustrated in Fig. 13, where we have plotted simulated

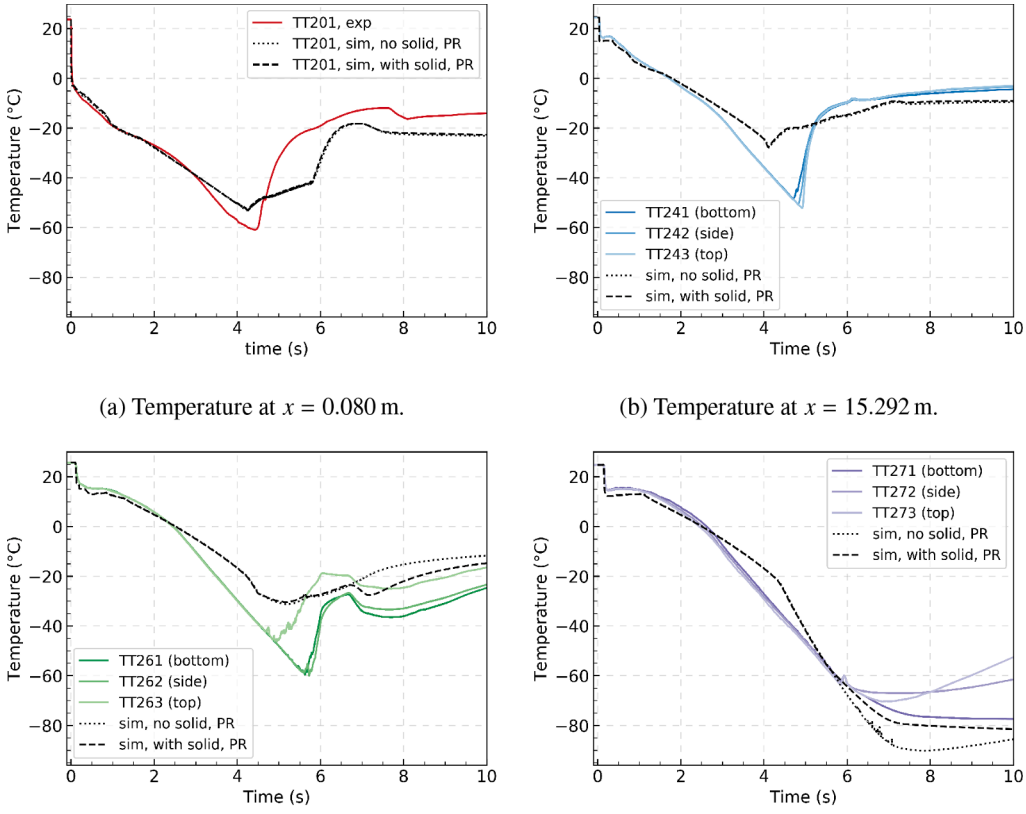

(a) Temperature at x = 0.080 m.

(b) Temperature at x = 15.292 m.

(c) Temperature at x = 46.085 m.

(d) Temperature at x = 61.280 m.

Fig. 12. Measured and simulated temperature for Test no. 9.

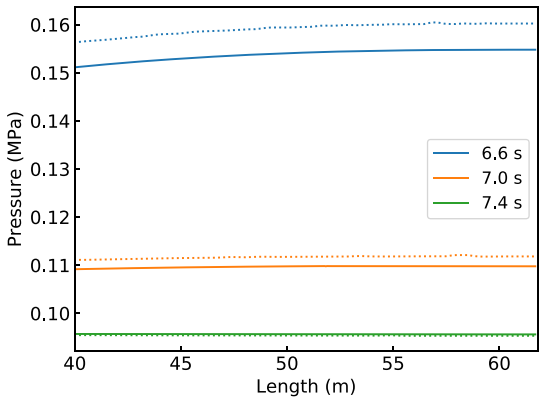

(a) Pressure.

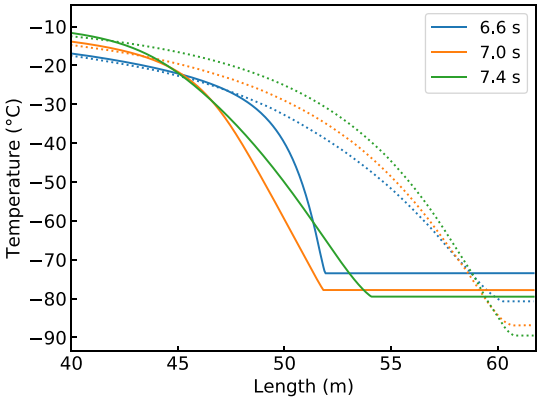

(b) Temperature.

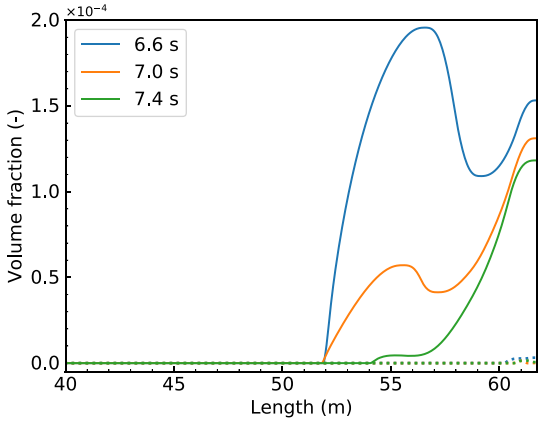

(c) Volume fractions. Solid lines: solid. Dotted lines: liquid.

Fig. 13. Simulated profiles for Test no. 9 at three times at the closed end of the pipe. The solid lines are simulated including the solid model, while the dotted lines are simulated without considering solid. The dotted lines have the same colouring as the solid lines.

profiles for pressure, temperature and volume fractions near the closed end of the tube. Simulation results obtained by including solid CO_2 in the model (full lines) and without a solid-CO_2 model (dotted lines) are shown. The profiles are plotted at a time before, at, and after the temperature drop seen in Fig. 12c at about 7 s.

Figure 13b displays the results for temperature. In the simulations not including solid CO_2, we observe a higher temperature due to a high calculated heat-transfer due to the boiling of liquid. At the time of the snapshots, most of the liquid has evaporated, but there is some left (Fig. 13c). In the simulations including solid, cold gaseous CO_2 flows downstream (to the left) from the closed end as the solid CO_2 sublimates. At the same time, the heat transfer into the fluid is high due to the low temperatures. From Fig. 13a it is seen that the pressure is decreasing, making the fluid colder. It is also seen that the pressure decrease is slowing down, and that the pipe is below atmospheric pressure at 7.4 s. The cooling effect due to pressure drop therefore stops, and the heat transfer increases due to the reduced temperature. In Fig. 13c (and 13b) it is seen that some time between 7.0 s and 7.4 s, the solid front starts moving towards the closed end as the solid sublimates. As an effect of these competing cooling and heating phenomena, the temperature does not increase monotonically with time after dry-out at positions in the vicinity of $x = 45$m.

At the closed end of the tube, the flow speed is naturally very low, so the trends are different from those at the downstream positions, as seen in Fig. 12d. The measured temperature (by all three sensors) shows a kink at -60 °C and 6 s, which we interpret to be due to the formation of solid CO_2. The measured temperature decreases somewhat below the triple-point temperature (-56.6 °C), after which it increases for a short while, possibly indicating non-equilibrium as solid CO_2 is formed. After this, the temperature at the bottom of the tube drops to about -78 °C, which indicates that some solid CO_2 remains there. Interestingly, after 6 s, the simulated temperature accounting for solid CO_2 agrees well with the experimental observation, whereas the temperature simulated without solid CO_2 drops too low, to about -90 °C.

The measured and simulated temperatures for Test 12 (CO_2-He) are displayed in Fig. 14. The comments made for Test 9 in the preceding paragraph also apply to this case, although we observe that dry-out and solid CO_2 formation occurs slightly earlier for CO_2-He than for CO_2-N_2.

In Fig. 15, we show the effect of impurities on temperature by plotting experimental results from the three experiments (CO_2, CO_2-N_2 and CO_2-He) for four different positions, 15 m from the open end (Fig. 15a), in the middle of the tube (Fig. 15b), 15 m from the closed end (Fig. 15c) and at the closed end (Fig. 15d). It can be seen that the minimum observed temperature decreases from about -50 °C close to the outlet to -78 °C at the closed end. The dry-out point (where the liquid has evaporated and the temperature starts rising) occurs somewhat later as one progresses upstream. The tendency is different at the closed end of the tube, where the temperature in the later part of the experiment is dominated by solid CO_2 – the vapour-solid equilibrium temperature is -78 °C at atmospheric pressure and it is not much

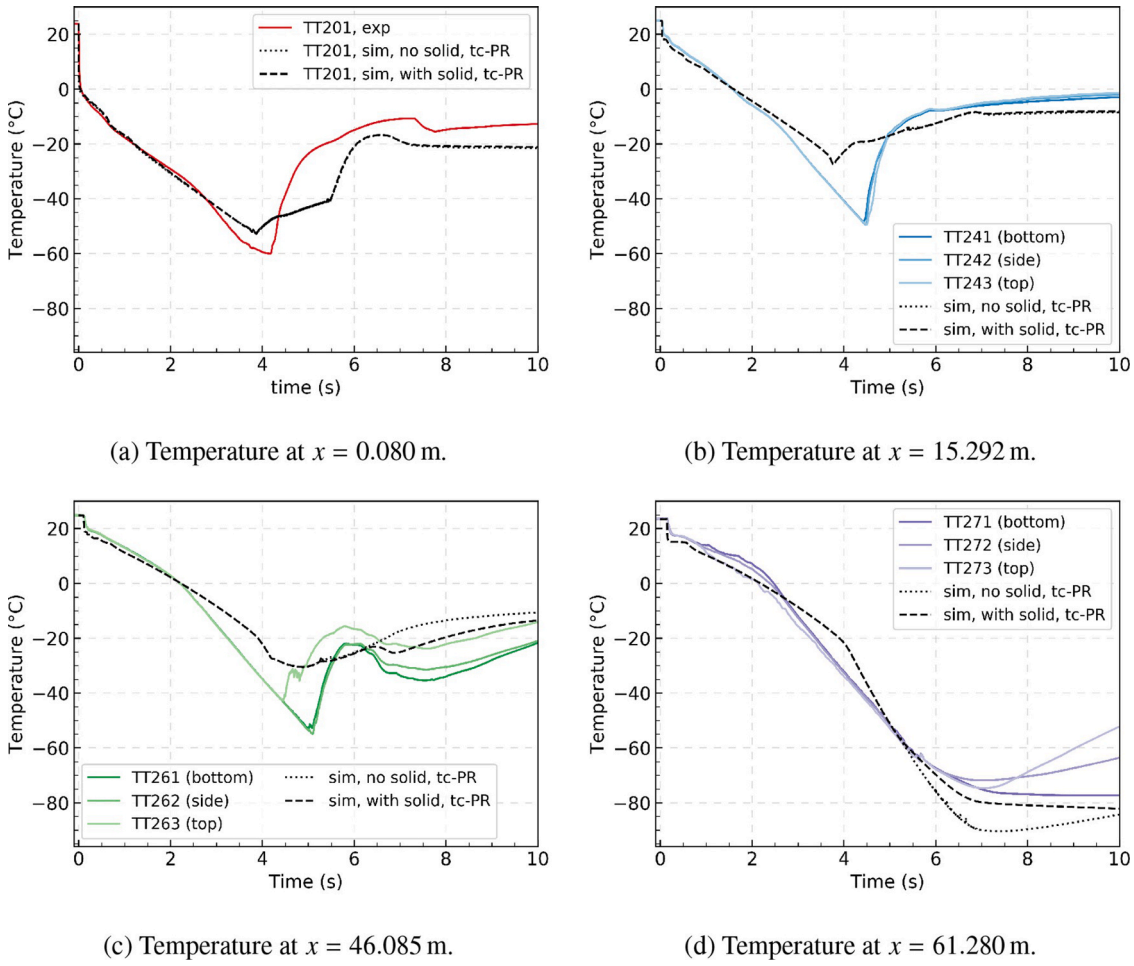

Fig. 14. Measured and simulated temperature for Test no. 12 (CO_2-He).

affected by the impurities. At all positions, Test 8 (pure CO_2) experiences the slowest cooling, with Test 9 (CO_2-N_2) in the middle and Test 12 (CO_2-He) with the fastest cooling. It is CO_2-He that experiences dry-out first (at 4.5 s at 15 m, followed by CO_2-N_2 at 5 s and CO_2 at 5.25 s. We can conclude that in the present case, the impurities affect the temperature dynamics, but not the 'worst case' coldest temperature.

5. Conclusion

The new ECCSEL Depressurization Facility has been commissioned for non-flammable impurities. We have reported and analysed two full-bore depressurization experiments of a tube, one with CO_2 with 1.8 mol % N_2 and one with 1.92 mol % He, comparing with a pure-CO_2 experiment from Munkejord et al. (2020a). In particular, both pressure and temperature data with high spatial and temporal resolution have been presented. The experiments show that the decompression behaviour of the CO_2 stream is significantly affected by impurities in this relatively moderate range. In addition, the decompression process is characterized by regimes of single-phase, two-phase (vapour-liquid and vapour-solid) and three-phase (vapour-solid-liquid) flow. As a consequence, simulation models used for considerations related to design and operation of CO_2 transport and injection systems should be able to accurately take these effects into account in order to enable safe and efficient CCS systems.

We observed an increase in the phase-transition pressure in the range of 1 MPa resulting from 1.8 mol % N_2, and almost 4 MPa resulting from 1.92 mol % He. This has consequences for systems where one for instance aims to avoid two-phase flow. For the rapid decompression relevant for the assessment of running-ductile fracture, we observed that the phase-transition pressure was significantly lower than the plateau (equilibrium) pressure. To physically model this non-equilibrium flow constitutes a challenging topic for further research.

For CO_2-N_2, the single-phase liquid decompression speed calculated using EOS-CG was in very good agreement with the experiments. For CO_2-He, on the other hand, neither the specially adapted tc-PR EOS nor the GERG-2008 EOS gave accurate results, the discrepancies being in the order of 10% for the decompression speed, depending on the pressure level.

For the early stage of depressurization, the pressure observed for pure CO_2 dropped fastest and that of CO_2-He slowest. However, after about 1.5 s, the situation was reversed, with the highest recorded pressure for pure CO_2 and the lowest for CO_2-He. This effect was reproduced by the HEM.

The impurities also affected the observed temperature dynamics. CO_2-N_2 gave a faster initial temperature drop and earlier dry-out than pure CO_2, and CO_2-He even more so.

We have implemented vapour-solid-liquid equilibrium calculations in conjunction with our HEM. Comparison with the experiments showed that in order to reproduce the correct temperature development, taking solid CO_2 into account was necessary both at the point where solid CO_2 was formed, and at downstream positions. At the closed end, failing to include solid CO_2 gave a too low calculated temperature, whereas 15 m downstream, it gave a too elevated temperature.

The HEM gave good temperature predictions close to the outlet, where the flow is highly dispersed, and at the closed end of the tube, where the temperature is governed mainly by the phase equilibria. In the

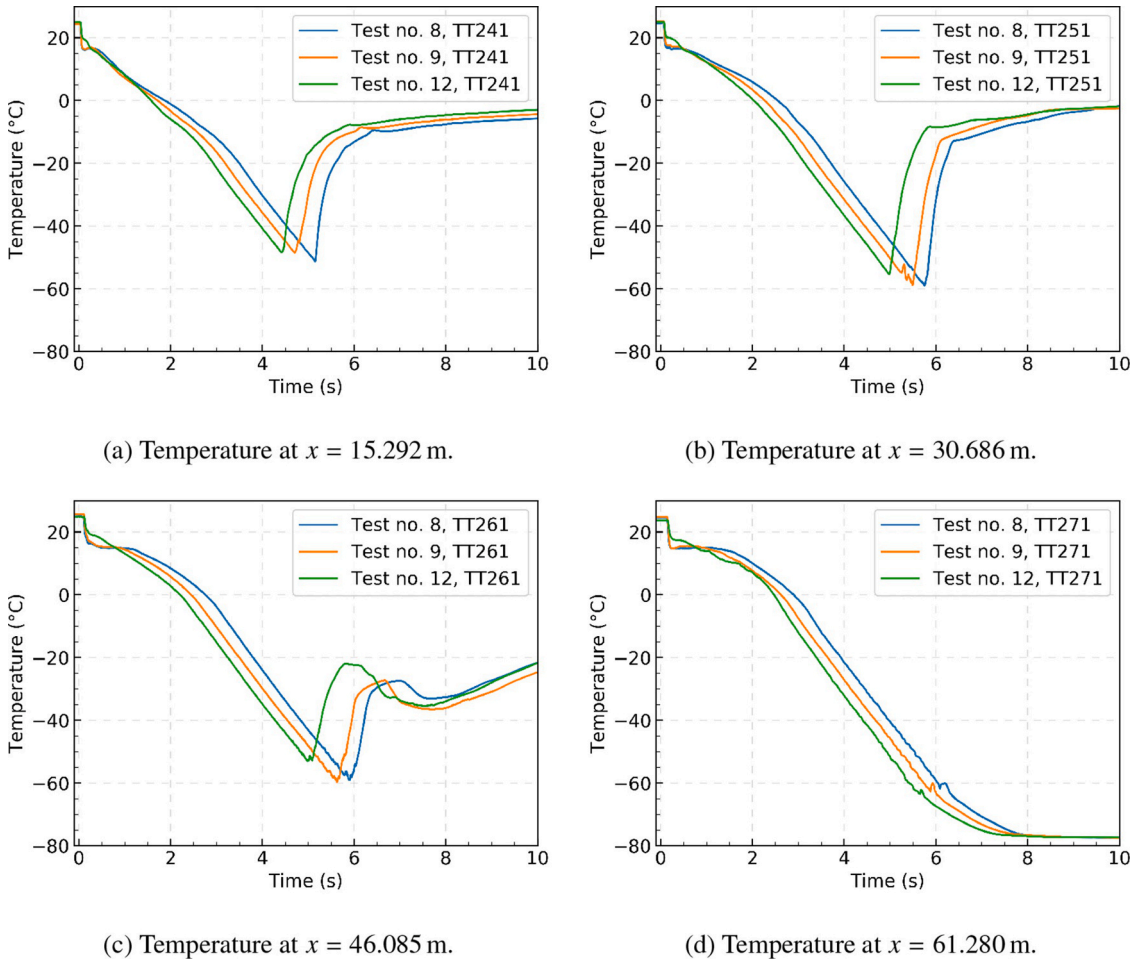

Fig. 15. Measured temperature for Test no. 8 (CO_2), 9 (CO_2-N_2) and 12 (CO_2-He).

middle of the tube, the HEM gave too early dry out, and a too high dry-out temperature. Improvements could perhaps be obtained by considering models including phase slip, as well as improved heat-transfer models.

Data availability

The experimental data recorded in this study can be downloaded from Zenodo (Munkejord et al., 2021).

CRediT authorship contribution statement

Svend Tollak Munkejord: Conceptualization, Methodology, Writing - original draft, Writing - review & editing, Supervision, Funding acquisition. **Han Deng:** Software, Formal analysis, Investigation, Data curation, Writing - original draft, Writing - review & editing, Visualization. **Anders Austegard:** Methodology, Software, Investigation, Resources, Writing - review & editing. **Morten Hammer:** Software, Investigation, Data curation, Writing - review & editing, Visualization. **Ailo Aasen:** Software, Investigation, Writing - original draft, Visualization. **Hans L. Skarsvåg:** Investigation, Project administration, Writing - review & editing.

Declaration of Competing Interest

The authors declare that they have no known competing financial interests or personal relationships that could have appeared to influence the work reported in this paper.

Acknowledgements

ACT ELEGANCY, Project No 271498, has received funding from DETEC (CH), BMWi (DE), RVO (NL), Gassnova (NO), BEIS (UK), Gassco, Equinor and Total, and is cofunded by the European Commission under the Horizon 2020 programme, ACT Grant Agreement No 691712.

The construction of the ECCSEL Depressurization Facility was supported by the INFRASTRUKTUR programme of the Research Council of Norway (225868).

We thank the anonymous reviewers, whose constructive comments helped improve the article.

References

Aakenes, F., 2012. Frictional pressure-drop models for steady-state and transient two-phase flow of carbon dioxide. Master's thesis, Department of Energy and Process Engineering, Norwegian University of Science and Technology (NTNU).

Aakenes, F., Munkejord, S.T., Drescher, M., 2014. Frictional pressure drop for two-phase flow of carbon dioxide in a tube: comparison between models and experimental data. Energy Procedia 51, 373–381. https://doi.org/10.1016/j.egypro.2014.07.044.

Armstrong, K., Allason, D., 2014. 2" NB Shocktube Releases of Dense Phase CO_2. Tech. rep. GL Noble Denton, Gilsland Cumbria, UK. Available from https://www.dnvgl.com/oilgas/innovation-development/joint-industry-projects/co2pipetrans.html

Aursand, E., Dumoulin, S., Hammer, M., Lange, H.I., Morin, A., Munkejord, S.T., Nordhagen, H.O., 2016. Fracture propagation control in CO_2 pipelines: validation of a coupled fluid-structure model. Eng. Struct. 123, 192–212. https://doi.org/10.1016/j.engstruct.2016.05.012.

Aursand, P., Hammer, M., Lavrov, A., Lund, H., Munkejord, S.T., Torsæter, M., 2017. Well integrity for CO_2 injection from ships: simulation of the effect of flow and material parameters on thermal stresses. Int. J. Greenh. Gas Con. 62, 130–141. https://doi.org/10.1016/j.ijggc.2017.04.007.

Aursand, P., Hammer, M., Munkejord, S.T., Wilhelmsen, O., 2013. Pipeline transport of CO_2 mixtures: models for transient simulation. Int. J. Greenh. Gas Con. 15, 174–185. https://doi.org/10.1016/j.ijggc.2013.02.012.

Bejan, A., 1993. Heat Transfer. John Wiley & Sons, Inc., New York. ISBN 0-471-50290-1

Botros, K.K., Geerligs, J., Rothwell, B., Carlson, L., Fletcher, L., Venton, P., 2010. Transferability of decompression wave speed measured by a small-diameter shock tube to full size pipelines and implications for determining required fracture propagation resistance. Int. J. Pres. Ves. Pip. 87 (12), 681–695. https://doi.org/10.1016/j.ijpvp.2010.10.006.

Botros, K.K., Geerligs, J., Rothwell, B., Robinson, T., 2016. Measurements of decompression wave speed in pure carbon dioxide and comparison with predictions by equation of state. J. Press. Vess. – T. ASME 138 (3). https://doi.org/10.1115/1.4031941.

Botros, K.K., Geerligs, J., Rothwell, B., Robinson, T., 2017. Effect of argon as the primary impurity in anthropogenic carbon dioxide mixtures on the decompression wave speed. Can. J. Chem. Eng. 95 (3), 440–448. https://doi.org/10.1002/cjce.22689.

Botros, K.K., Geerligs, J., Rothwell, B., Robinson, T., 2017. Measurements of decompression wave speed in binary mixtures of carbon dioxide mixtures and impurities. J. Press. Vess. – T. ASME 139 (2). https://doi.org/10.1115/1.4034016.

Botros, K.K., Geerligs, J., Rothwell, B., Robinson, T., 2017. Measurements of decompression wave speed in simulated anthropogenic carbon dioxide mixtures containing hydrogen. J. Press. Vess. – T. ASME 139 (2). https://doi.org/10.1115/1.4034466.

Botros, K.K., Geerligs, J., Zhou, J., Glover, A., 2007. Measurements of flow parameters and decompression wave speed following rupture of rich gas pipelines, and comparison with GASDECOM. Int. J. Pres. Ves. Pip. 84 (6), 358–367. https://doi.org/10.1016/j.ijpvp.2007.01.005.

Botros, K.K., Hippert Jr., E., Craidy, P., 2013. Measuring decompression wave speed in CO_2 mixtures by a shock tube. Pipelines Int. 16, 22–28.

Brown, S., Martynov, S., Mahgerefteh, H., Chen, S., Zhang, Y., 2014. Modelling the non-equilibrium two-phase flow during depressurisation of CO_2 pipelines. Int. J. Greenh. Gas Con. 30, 9–18. https://doi.org/10.1016/j.ijggc.2014.08.013.

Brown, S., Martynov, S., Mahgerefteh, H., Proust, C., 2013. A homogeneous relaxation flow model for the full bore rupture of dense phase CO_2 pipelines. Int. J. Greenh. Gas Con. 17, 349–356. https://doi.org/10.1016/j.ijggc.2013.05.020.

Burfield, D.W., Richardson, H.P., Guereca, R.A., 1970. Vapor-liquid equilibria and dielectric constants for the helium-carbon dioxide system. AIChE J. 16 (1), 97–100. doi:10.1002/aic.690160119.

Cao, Q., Yan, X., Guo, X., Zhu, H., Liu, S., Yu, J., 2018. Temperature evolution and heat transfer during the release of CO_2 from a large-scale pipeline. Int. J. Greenh. Gas Con. 74, 40–48. https://doi.org/10.1016/j.ijggc.2018.04.015.

Clausen, S., Oosterkamp, A., Strøm, K.L., 2012. Depressurization of a 50 km long 24 inches CO_2 pipeline. In: Røkke, N.A., Hägg, M.-B., Mazzetti, M.J. (Eds.), 6th Trondheim Conference on CO_2 Capture, Transport and Storage (TCCS-6). BIGCCS / SINTEF / NTNU, Energy Procedia vol. 23, Trondheim, Norway, pp. 256–265. https://doi.org/10.1016/j.egypro.2012.06.044.

Cosham, A., Jones, D.G., Armstrong, K., Allason, D., Barnett, J., 2012. The decompression behaviour of carbon dioxide in the dense phase. 9th International Pipeline Conference, IPC2012. ASME, IPTI, Calgary, Canada, vol. 3, pp. 447–464. https://doi.org/10.1115/IPC2012-90461.

DNV, 2012. Submarine Pipeline Systems. Offshore standard DNV-OS-F-101.

Drescher, M., Varholm, K., Munkejord, S.T., Hammer, M., Held, R., de Koeijer, G., 2014. Experiments and modelling of two-phase transient flow during pipeline depressurization of CO_2 with various N_2 compositions. In: Dixon, T., Herzog, H., Twinning, S. (Eds.), GHGT-12 – 12th International Conference on Greenhouse Gas Control Technologies. University of Texas at Austin / IEAGHGT, Energy Procedia, vol. 63, Austin, Texas, USA, pp. 2448–2457. https://doi.org/10.1016/j.egypro.2014.11.267.

ECCSEL, 2020. Depressurization facility. https://www.eccsel.org/facilities/transport/no25_sintef_er_depress/. Accessed 2020-03-31.

Edenhofer, O., Pichs-Madruga, R., Sokona, Y., Farahani, E., Kadner, S., Seyboth, K., Adler, A., Baum, I., Brunner, S., Eickemeier, P., Kriemann, B., Savolainen, J., Schlømer, S., von Stechow, C., Zwickel, T.J.M., 2014. Climate change 2014: mitigation of climate change. Tech. rep. Working Group III Contribution to the Fifth Assessment Report of the Intergovernmental Panel on Climate Change, Summary for Policymakers, IPCC..http://mitigation2014.org/

Ely, J.F., Hanley, H.J.M., 1981. Prediction of transport properties. 1. Viscosity of fluids and mixtures. Ind. Eng. Chem. Fund. 20 (4), 323–332. https://doi.org/10.1021/i100004a004.

Ely, J.F., Hanley, H.J.M., 1983. Prediction of transport properties. 2. Thermal conductivity of pure fluids and mixtures. Ind. Eng. Chem. Fund. 22 (1), 90–97. https://doi.org/10.1021/i100009a016.

Equinor, 2019. Northern Lights Project Concept Report.Available from https://northernlightsccs.com/assets/documents/Northern-Lights-Project-Concept-report.pdf

Friedel, L., 1979. Improved friction pressure drop correlations for horizontal and vertical two phase pipe flow. Proceedings, European Two Phase Flow Group Meeting. Ispra, Italy. Paper E2.

Gernert, J., Span, R., 2016. EOS-CG: A Helmholtz energy mixture model for humid gases and CCS mixtures. J. Chem. Thermodyn. 93, 274–293. https://doi.org/10.1016/j.jct.2015.05.015.

Gu, S., Li, Y., Teng, L., Wang, C., Hu, Q., Zhang, D., Ye, X., Wang, J., Iglauer, S., 2019. An experimental study on the flow characteristics during the leakage of high pressure CO_2 pipelines. Process Saf. Environ. 125, 92–101. https://doi.org/10.1016/j.psep.2019.03.010.

Gungor, K.E., Winterton, R.H.S., 1987. Simplified general correlation for saturated flow boiling and comparisons of correlations with data. Chem. Eng. Res. Des. 65 (2), 148–156.

Guo, X., Yan, X., Yu, J., Yang, Y., Zhang, Y., Chen, S., Mahgerefteh, H., Martynov, S., Collard, A., 2017. Pressure responses and phase transitions during the release of high pressure CO_2 from a large-scale pipeline. Energy 118, 1066–1078. https://doi.org/10.1016/j.energy.2016.10.133.

Guo, X., Yan, X., Yu, J., Zhang, Y., Chen, S., Mahgerefteh, H., Martynov, S., Collard, A., Proust, C., 2016. Pressure response and phase transition in supercritical CO_2 releases from a large-scale pipeline. Appl. Energy 178, 189–197. https://doi.org/10.1016/j.apenergy.2016.06.026.

Hammer, M., Aasen, A., Wilhelmsen, O., 2020. Thermopack. https://github.com/SINTEF/thermopack/. Accessed 2020-12-15.

Hammer, M., Ervik, A., Munkejord, S.T., 2013. Method using a density-energy state function with a reference equation of state for fluid-dynamics simulation of vapor-liquid-solid carbon dioxide. Ind. Eng. Chem. Res. 52 (29), 9965–9978. https://doi.org/10.1021/ie303516m.

Huh, C., Cho, M.-I., Hong, S., Kang, S.G., 2014. Effect of impurities on depressurization of CO_2 pipeline transport. In: Dixon, T., Herzog, H., Twinning, S. (Eds.), GHGT-12 – 12th International Conference on Greenhouse Gas Control Technologies. University of Texas at Austin / IEAGHGT, Energy Procedia, vol. 63, Austin, Texas, USA, pp. 2583–2588. https://doi.org/10.1016/j.egypro.2014.11.280.

IEA, 2017. Energy technology perspectives. ISBN 978-92-64-27597-3. doi:10.1787/energy_tech-2017-en.

Jäger, A., Span, R., 2012. Equation of state for solid carbon dioxide based on the Gibbs free energy. J. Chem. Eng. Data 57 (2), 590–597. https://doi.org/10.1021/je2011677.

Jie, H.E., Xu, B.P., Wen, J.X., Cooper, R., Barnett, J., 2012. Predicting the decompression characteristics of carbon dioxide using computational fluid dynamics. 9th International Pipeline Conference IPC2012. ASME, IPTI, Calgary, Canada, pp. 585–595. https://doi.org/10.1115/IPC2012-90649.

Jones, D.G., Cosham, A., Armstrong, K., Barnett, J., Cooper, R., 2013. Fracture-propagation control in dense-phase CO_2 pipelines. 6th International Pipeline Technology Conference. Lab. Soete and Tiratsoo Technical, Ostend, Belgium. Paper no. S06-02

Kesselman, P.M., Alekseenko, G.P., 1974. Experimental investigation of the compressibility of mixtures of carbon dioxide and helium. Therm. Eng. 21, 102–105.

Kosov, N.D., Brovanov, I.S., 1975. The compressibility of binary mixtures of helium, nitrogen and argon with carbon dioxide from 5.9 to 59.0 megapascals. Therm. Eng. 22, 77–79.

Kunz, O., Wagner, W., 2012. The GERG-2008 wide-range equation of state for natural gases and other mixtures: an expansion of GERG-2004. J. Chem. Eng. Data 57 (11), 3032–3091. https://doi.org/10.1021/je300655b.

Le Guennec, Y., Lasala, S., Privat, R., Jaubert, J.N., 2016. A consistency test for α-functions of cubic equations of state. Fluid Phase Equilib. 427, 513–538. https://doi.org/10.1016/j.fluid.2016.07.026.

Le Guennec, Y., Privat, R., Jaubert, J.N., 2016. Development of the translated-consistent tc-PR and tc-RK cubic equations of state for a safe and accurate prediction of volumetric, energetic and saturation properties of pure compounds in the sub-and super-critical domains. Fluid Phase Equilib. 429, 301–312. https://doi.org/10.1016/j.fluid.2016.09.003.

Liu, K. F., 1969. Phase equilibria in the helium-carbon dioxide, -argon, -methane, -nitrogen, and -oxygen systems. PhD thesis, Georgia Institute of Technology, Atlanta GA.

Mackendrick, R.F., Heck, C.K., Barrick, P.L., 1968. Liquid-vapor equilibriums of the helium-carbon dioxide system. J. Chem. Eng. Data 13 (3), 352–353.doi:10.1021/je60038a014.

Mahgerefteh, H., Brown, S., Denton, G., 2012. Modelling the impact of stream impurities on ductile fractures in CO_2 pipelines. Chem. Eng. Sci. 74, 200–210. https://doi.org/10.1016/j.ces.2012.02.037.

Mahgerefteh, H., Brown, S., Martynov, S., 2012. A study of the effects of friction, heat transfer, and stream impurities on the decompression behavior in CO_2 pipelines. Greenh. Gas. Sci. Tech. 2 (5), 369–379. https://doi.org/10.1002/ghg.1302.

Martynov, S., Zheng, W., Mahgerefteh, H., Brown, S., Hebrard, J., Jamois, D., Proust, C., 2018. Computational and experimental study of solid-phase formation during the decompression of high-pressure CO_2 pipelines. Ind. Eng. Chem. Res. 57 (20), 7054–7063. https://doi.org/10.1021/acs.iecr.8b00181.

Michelsen, M.L., Mollerup, J.M., 2007. Thermodynamic Models: Fundamentals & Computational Aspects, second ed. Tie-Line Publications, Holte, Denmark. ISBN 87-989961-3-4

Moe, A.M., Dugstad, A., Benrath, D., Jukes, E., Anderson, E., Catalanotti, E., Durusut, E., Neele, F., Grunert, F., Mahgerefteh, H., Gazendam, J., Barnett, J., Hammer, M., Span, R., Brown, S., Munkejord, S.T., Weber, V., 2020. A trans-european CO_2 transportation infrastructure for CCUS: Opportunities & challenges. Report. Zero Emissions Platform, Brussels, Belgium.Available from https://zeroemissionsplatform.eu/wp-content/uploads/A-Trans-European-CO2-Transportation-Infrastructure-for-CCUS-Opportunities-Challenges.pdf

Munkejord, S.T., Austegard, A., Deng, H., Hammer, M., Stang, H.G.J., Løvseth, S.W., 2020. Depressurization of CO_2 in a pipe: high-resolution pressure and temperature data and comparison with model predictions. Energy 211, 118560. https://doi.org/10.1016/j.energy.2020.118560.

Munkejord, S.T., Deng, H., Austegard, A., Hammer, M., Skarsvåg, H.L., Aasen, A., 2021. Depressurization of CO_2-N_2 and CO_2-He in a pipe: experiments and modelling of pressure and temperature dynamics – dataset. Zenodo. https://doi.org/10.5281/zenodo.3984822.

Munkejord, S.T., Hammer, M., 2015. Depressurization of CO_2-rich mixtures in pipes: two-phase flow modelling and comparison with experiments. Int. J. Greenh. Gas Con. 37, 398–411. https://doi.org/10.1016/j.ijggc.2015.03.029.

Munkejord, S.T., Hammer, M., Løvseth, S.W., 2016. CO_2 transport: data and models – a review. Appl. Energy 169, 499–523. https://doi.org/10.1016/j.apenergy.2016.01.100.

Péneloux, A., Rauzy, E., Fréze, R., 1982. A consistent correction for Redlich-Kwong-Soave volumes. Fluid Phase Equilib. 8 (1), 7–23. https://doi.org/10.1016/0378-3812(82)80002-2.

Peng, D.Y., Robinson, D.B., 1976. A new two-constant equation of state. Ind. Eng. Chem. Fund. 15 (1), 59–64. https://doi.org/10.1021/i160057a011.

Porter, R.T.J., Fairweather, M., Pourkashanian, M., Woolley, R.M., 2015. The range and level of impurities in CO_2 streams from different carbon capture sources. Int. J. Greenh. Gas Con. 36, 161–174. https://doi.org/10.1016/j.ijggc.2015.02.016.

Shafiq, U., Shariff, A.M., Babar, M., Azeem, B., Ali, A., Bustam, M.A., 2020. A review on modeling and simulation of blowdown from pressurized vessels and pipelines. Process Saf. Environ. 133, 104–123. https://doi.org/10.1016/j.psep.2019.10.035.

Span, R., Eckermann, T., Herrig, S., Hielscher, S., Jäger, A., Thol, M., 2016. TREND. Thermodynamic Reference and Engineering Data 3.0. Lehrstuhl für Thermodynamik. Ruhr-Universität Bochum.

Streb, A., Hefti, M., Gazzani, M., Mazzotti, M., 2019. Novel adsorption process for co-production of hydrogen and CO_2 from a multicomponent stream. Ind. Eng. Chem. Res. 58 (37), 17489–17506. https://doi.org/10.1021/acs.iecr.9b02817.

Teng, L., Li, Y., Zhao, Q., Wang, W., Hu, Q., Ye, X., Zhang, D., 2016. Decompression characteristics of CO_2 pipelines following rupture. J. Nat. Gas Sci. Eng. 36 (A), 213–223. https://doi.org/10.1016/j.jngse.2016.10.026.

Toro, E.F., Billett, S.J., 2000. Centred TVD schemes for hyperbolic conservation laws. IMA J. Numer. Anal. 20 (1), 47–79. https://doi.org/10.1093/imanum/20.1.47.

Twu, C.H., Bluck, D., Cunningham, J.R., Coon, J.E., 1991. A cubic equation of state with a new alpha function and a new mixing rule. Fluid Phase Equilib. 69, 33–50. https://doi.org/10.1016/0378-3812(91)90024-2.

Wilhelmsen, O., Aasen, A., Skaugen, G., Aursand, P., Austegard, A., Aursand, E., Gjennestad, M.A., Lund, H., Linga, G., Hammer, M., 2017. Thermodynamic modeling with equations of state: present challenges with established methods. Ind. Eng. Chem. Res. 56 (13), 3503–3515. https://doi.org/10.1021/acs.iecr.7b00317.

Yan, X., Guo, X., Yu, J., Chen, S., Zhang, Y., Mahgerefteh, H., Martynov, S., Brown, S., 2018. Flow characteristics and dispersion during the vertical anthropogenic venting of supercritical CO_2 from an industrial scale pipeline. In: Yan, J., Feitz, A., Li, X., Zhang, X. (Eds.), Applied Energy Symposium and Forum, Carbon Capture, Utilization and Storage, CCUS 2018. Energy Procedia, vol. 154, Perth, Australia, pp. 66–72. https://doi.org/10.1016/j.egypro.2018.11.012.

Zheng, W., Mahgerefteh, H., Martynov, S., Brown, S., 2017. Modeling of CO_2 decompression across the triple point. Ind. Eng. Chem. Res. 56 (37), 10491–10499. https://doi.org/10.1021/acs.iecr.7b02024.